

REPORT DOCUMENTATION PAGE			Form Approved OMB No. 0704-0188	
Public reporting burden for this collection of information is estimated to average 1 hour per response, including the time for reviewing instructions, searching existing data sources, gathering and maintaining the data needed, and completing and reviewing the collection of information. Send comments regarding this burden estimate or any other aspect of this collection of information, including suggestions for reducing this burden, to Washington Headquarters Services, Directorate for Information Operations and Reports, 1215 Jefferson Davis Highway, Suite 1204, Arlington, VA 22202-4302, and to the Office of Management and Budget, Paperwork Reduction Project (0704-0188), Washington, DC 20503.				
1. AGENCY USE ONLY (Leave blank)		2. REPORT DATE	3. REPORT TYPE AND DATES COVERED Final Report 6/15/01 - 12/14/03	
4. TITLE AND SUBTITLE IP3 Predictions Based on Monte Carlo Transport Studies of GaN High Electron Mobility Transistors (HEMTs)			5. FUNDING NUMBERS DAAD19-01-1-0617, Modification P00001	
6. AUTHORS Ravindra P. Joshi, Old Dominion University				
7. PERFORMING ORGANIZATION NAME(S) AND ADDRESS(ES) Old Dominion University Research Foundation 800 W. 46 th Street, P.O. Box 6369 Norfolk, VA 23508			8. PERFORMING ORGANIZATION REPORT NUMBER 41419-EL 2004 MAR 2	
9. SPONSORING/MONITORING AGENCY NAME(S) AND ADDRESS(ES) U.S. Army Research Office P.O. Box 12211 RTP, NC 27709-2211			10. SPONSORING/MONITORING AGENCY REPORT NUMBER 41419.5-EL MIG-58	
11. SUPPLEMENTARY NOTES				
12a. DISTRIBUTION/AVAILABILITY STATEMENT Approved for Public Release unlimited Availability			12b. DISTRIBUTION CODE	
13. ABSTRACT (Maximum 200 words) Calculations of the electronic mobility and drift velocity have been carried out for bulk GaN and AlGaIn-GaN heterojunctions based on a Monte Carlo approach. Very good agreement with available experiments has been obtained, and the calculations yielded a set of best-fit transport parameters. The calculations were then extended for the large-signal nonlinear response characteristics of HEMTs with particular emphasis on inter-modulation distortion (IMD). The results demonstrated an optimal operating point for low IMD at reasonably large output power due to a minima in the IMD curve. An increase in dynamic range with temperature has been predicted, due to a relative suppression of interface roughness scattering. The results indicate increasing the mole fraction for the barrier layer, reducing the transit length, and introducing a thin AlN interfacial layer for suppressing real space transfer performance enhancements. Simulations were also carried out to probe possible enhancements in Gun effect oscillators. It has been shown that repetitive structures with serial segments to fashion a "multiple domain" device could lead to significant improvements in output power over conventional, single-transit structure, and so such multiple GaN diodes merit serious experimental study. Monte Carlo studies of GaN HEMTs also probed the effects of scattering due to edge dislocations strains. For self-consistency, numerical solution of Schrödinger, Poisson, and charge balance equations were used for the eigen-functions. Electron mobilities predictions around $1.711 \times 10^3 \text{ cm}^2/\text{Vs}$, are in close agreement with reported data. At the highest dislocation density of 10^{10} cm^{-2} , mobility reductions of 16.8 percent and 8.6 percent are predicted for 77 K and 300 K, respectively.				
14. SUBJECT TERMS 20040401 022			15. NUMBER OF PAGES 43	
			16. PRICE CODE	
17. SECURITY CLASSIFICATION OF REPORT Unclassified	18. SECURITY CLASSIFICATION OF THIS PAGE Unclassified	19. SECURITY CLASSIFICATION OF ABSTRACT Unclassified	20. LIMITATION OF ABSTRACT SAR	

Monte Carlo Transport Studies of GaN High Electron Mobility Transistors (HEMTs) for Microwave Applications

**Principal Investigator: Ravindra P. Joshi
Department of Electrical and Computer Engineering
Old Dominion University, Norfolk, VA 23529-0246**

FINAL REPORT TO U. S. ARMY RESEARCH OFFICE

March, 2004.

Abstract

Calculations of the electronic mobility and drift velocity were carried out for bulk GaN and AlGaIn-GaN heterojunctions based on a Monte Carlo approach. Very good agreement with available experiments was obtained, and the calculations yielded a set of best-fit transport parameters. The calculations were then extended for the large-signal nonlinear response characteristics of HEMTs with particular emphasis on intermodulation distortion (IMD). The results demonstrated an optimal operating point for low IMD at reasonably large output power due to a minima in the IMD curve. An increase in dynamic range with temperature has been predicted, due to a relative suppression of interface roughness scattering. The results indicate increasing the mole fraction for the barrier layer, reducing the transit length, and introducing a thin AlN interfacial layer for suppressing real space transfer performance enhancements.

Simulations were also carried out to probe possible enhancements in Gunn effect oscillators. It has been shown that repetitive structures with serial segments to fashion a "multiple domain" device could lead to significant improvements in output power over conventional, single-transit structure, and so such multiple GaN diodes merit serious experimental study. Monte Carlo studies of GaN HEMTs also probed the effects of scattering due to edge dislocations strains. For self-consistency, numerical solution of Schrödinger, Poisson, and charge balance equations were used for the eigen-functions. Electron mobilities predictions around $1.711 \times 10^3 \text{ cm}^2/\text{Vs}$, are in close agreement with reported data. At the highest dislocation density of 10^{10} cm^{-2} , mobility reductions of 16.8 percent and 8.6 percent are predicted for 77 K and 300 K, respectively.

DISTRIBUTION STATEMENT A
Approved for Public Release
Distribution Unlimited

1. INTRODUCTION

Over the past five years or so, the nitride material system has been the focus of intense research.¹⁻⁸ Advantages of these direct, large-bandgap materials include the ability to sustain large electric fields ($\sim 10^8 \text{ Vm}^{-1}$, which bodes well for device downscaling and higher breakdown voltage), high saturation velocities ($\sim 1.5 \times 10^5 \text{ ms}^{-1}$), lower generation noise, radiation hardness, and high-temperature operation. GaN-based electronic amplifiers are projected to have significant improvement over silicon devices.⁹ The nitrides have also shown promise as emitters and detectors¹⁰⁻¹², Bragg reflectors,¹³ light-emitting diodes (LEDs),¹⁴ sensors for jet and automobile engines,¹⁵ and space-based operation in the solar blind region ($\sim 260 - 290 \text{ nm}$).

The high-field drift velocity of bulk GaN is larger than that of GaAs^{16,17} due to the higher inter-valley separation and the larger optical phonon energy. GaN lends itself to hetero-structure fabrication, and the presence of a strong internal polarization can create very high sheet carrier densities ($> 10^{17} \text{ m}^{-2}$). Experimental demonstrations of large radio-frequency (RF) power densities, as measured in Watts per millimeter of the gate periphery, have already been made¹⁸⁻²¹. The higher thermal conductivity of GaN relative to GaAs and use of SiC substrates^{22,23} should help alleviate the thermal management issue. These aspects collectively enhance the prospects of GaN for microwave power amplification, particularly at the X-band and higher frequencies.²⁴⁻²⁶

Regarding electron transport properties, the Σ -valley effective mass of GaN is 0.22, which is about three times higher than that of GaAs. Hence, the mobility in bulk GaN is expected to be inferior to GaAs, and this has been shown in experimental work. However, the high-field drift velocity of bulk GaN is larger than that of GaAs.^{27,28} This is due to the higher inter-valley separation and the larger energy of optical phonons. The former helps keep a higher fraction of electrons within the lower mass valley, while the latter reduces the net role of phonon scattering by increasing the emission threshold. A more striking advantage for GaN, however, results upon carrier confinement that leads to the creation of a two-dimensional electron gas (2DEG). Carrier confinement is typically engineered through the use of single or double modulation-doped heterostructures²⁹. This, as proposed originally for the GaAs system, leads to the physical separation of the mobile electrons from their parent donors, thereby reducing impurity scattering. In GaN,

however, the presence of a strong internal polarization arising from the spontaneous and piezoelectric effects works to create stronger band bending and contributes to very high sheet carrier densities, even in the absence of intentional doping. Characterization of the heterojunction field-effect transistors (HFETs) fabricated has revealed strong enhancement in carrier densities,³ which should lead to higher currents. The ac gain is therefore expected to be large, and so GaN HFETs offer bright prospects for use in microwave amplification, particularly at the *X*-band and higher frequencies.^{29,30}

Polarization arises in GaN due to its non centro-symmetric atomic arrangement. The nitrides exhibit large piezoelectric effects under stress along the *c*-direction due to the large lattice mismatch. Piezoelectric coefficients are almost an order of magnitude larger than the traditional III-V materials.³¹ Such polarization can cause a sizeable Stark shift in quantum wells^{32,33} and works to alter the interfacial concentration of free carriers in strained zincblende GaN grown along the (111) orientation³⁴ or in pseudomorphic wurtzite material grown in the (0001) orientation.³⁵ Carrier densities as high as $4 \times 10^{13} \text{ cm}^{-2}$ have been reported, even in the absence of doping within the barrier layer.³⁶ In addition to strain-related electric fields, a large spontaneous polarization exists, even at zero strain, as pointed out by Bernardini et al.³⁷ Aluminum nitride, for example, possesses a spontaneous polarization that is only about 3 times smaller than that of a typical ferroelectric perovskite.³⁸ Hence, interface fields as high as 2 MV/cm can result.

A number of issues somewhat unique to the GaN-based heterostructure system arise and can be expected to have important bearing on the transport behavior. The first issue is related to the large polarization. For instance, polarization-related modifications to the internal fields could affect ionization rates in quantum-well devices³⁹ or alter electronic injection at the gate contacts of HFETs.⁴⁰ Furthermore, carrier mobility should also be affected by the polarization-induced field enhancements, since carrier wave functions and the scattering rates are directly modified in the process. In addition, interface roughness scattering is expected to increase due to the close proximity of the 2DEG, with the barrier layer at the higher electric fields. The interface roughness scattering is typically quantified on the basis of weak-perturbation theory, in terms of two parameters: the root-mean-square value of fluctuations at the interface σ , and the correlation length L between fluctuations. These parameter values are not well known for

AlGaIn/GaN HFETs and need to be determined. It is also unclear whether weak perturbation theory would be adequate for accurately predicting the transport behavior. Screening effects arising from the higher electron density also need to be considered in evaluating the transport properties. These could exhibit spatial inhomogeneity across the interface. Next, the degeneracy effects associated with the higher electron density need to be carefully evaluated because of the high 2DEG density. There have been no studies into the role and extent of Pauli exclusion on the mobility in GaN HFETs, to the best of our knowledge. A third point relates to the impact of material parameters and geometry on the electrical response. For example, changes in the mole fraction of the AlGaIn barrier layer, the spacer thickness, or the barrier width all alter the polarization field, the carrier density, and, thus, the electrical response characteristics. It is important to obtain quantitative predictions in order to optimize the device operating characteristics. Finally, numerical evaluations of the drift velocity as a function of the applied gate voltage and longitudinal field need to be carried out to ascertain the nonlinearity in response and the high-temperature behavior. Changes in the interface field with gate bias, for example, are expected to produce nonlinear variations in drift velocity. Such nonlinearity can lead to possible harmonic generation, intermodulation and mixing of time-dependent signals applied to the gate of HFET structures.

One of the most important requirements for microwave power amplifiers is the level of nonlinear distortion and their inter-modulation (IM) behavior. Nonlinearity in the output current response with applied gate voltage results from the combined nonlinear behaviors of carrier drift velocity and the channel density. The scattering rates, which control drift velocity, are nonlinear functions of energy. For example, interface roughness scattering exhibits a nonlinear increase with gate bias⁴¹ due to the increased proximity of the two-dimensional electron gas (2DEG) with the barrier layer. The gate voltage (V_G) dependent variations in the 2DEG density, also affect scattering through changes in the screening of polar interactions and the degeneracy level.⁴¹ Carrier density dependence on the mole fraction, barrier thickness,⁴² and real space transfer into AlGaIn, which depends on both the gate and drain bias levels, all work to modify the transport characteristics further.

Since the satellite valley effective electronic masses of both zincblende and wurtzite-phase GaN are higher than in the lowest conduction bands, the material appears to show promise as a large-signal oscillator based on the transferred electron effect.⁴³ The presence of an inflection point in the $\bar{\epsilon}_1$ -valley bandstructure of the zincblende phase has also been suggested as a source of negative differential resistance (NDR)⁴⁴. As compared to the traditional GaAs and InP-based negative differential resistance (NDR) devices,⁴⁵⁻⁴⁶ the conversion efficiency and power handling capacity should be superior. Despite the potential, there have not been many studies on this subject to the best of our knowledge. The only reports appear to be by Alekseev and Pavlidis⁴³ for wurtzite GaN based on transient hydrodynamic simulations, and by Zhao et al.⁴⁷ for the zincblende phase. A full Monte Carlo treatment of the time-dependent transferred electron problem, is more accurate and desirable than the hydrodynamic scheme. Previous studies have often used the steady-state velocity-field characteristics⁴⁸ and relied on somewhat older band structure data. For example, previous reports were based on $\bar{\epsilon}_1$ - $\bar{\epsilon}_2$ and M-L intervalley separations of 1.9 eV and 2.1 eV, respectively^{49,50}. More recent calculations⁵¹ suggest a $\bar{\epsilon}_1$, M-L, $\bar{\epsilon}_3$, L_1 , A_1 ordering, with the two lowest valleys 2.2717 eV and 2.4 eV above $\bar{\epsilon}_1$. In view of this, it is perhaps important to re-examine the large-signal response characteristics of GaN-based oscillators based on recent data.

2. MONTE CARLO SIMULATIONS

2.1 Bulk GaN Material

The simulation scheme for bulk wurtzite GaN is discussed first. Details of the Monte Carlo approach are similar to those described previously.⁴ A three-valley, nonparabolic conduction band model was used for the transport calculations in bulk GaN. For wurtzite-phase GaN, the minimum is located at the $\bar{\epsilon}$ -point. The satellite valleys are at the U -point that is two-thirds of the way between the L - and M - symmetry points. The next highest valley is located at the $\bar{\epsilon}_3$ -point. Thus, two $\bar{\epsilon}$ -valleys and the six equivalent U -valleys were considered. A three-dimensional view of the Brillouin zone including points within the irreducible wedge is shown in Fig. 1. The effective masses have been calculated to be 0.2283 and 0.1846 along the perpendicular and parallel directions, respectively, with a non-parabolicity coefficient of about 0.37 eV⁻¹. The satellite valleys

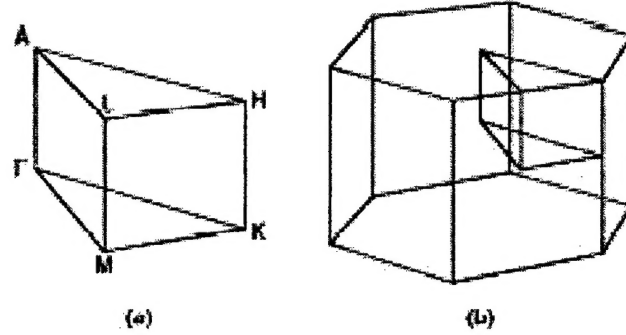


Fig. 1. (a) Brillouin zone schematic including the various symmetry points within the irreducible wedge. (b) View of the full brillouin zone including the irreducible wedge.

are at the U -point that is two-thirds of the way between the L- and M- symmetry points, with an energy separation of 2.2717 eV. According to the calculations by Goano et al.⁵¹, the next highest valley is located at the ϵ_3 -point, 2.4 eV above ϵ_3 . Finally, the valleys at the L_1 and A_1 points are located 2.5 eV and 2.6 eV, respectively above the conduction band minima. The effective masses for the M-L minima are anisotropic. As given in Table I the mass is 3.0375 (along ϵ - A_1), 0.3158 (along K-H), and 0.3858 (along the M and L points). The corresponding nonparabolicity coefficients also depend on the direction, and are reported to be: -1.0325 eV^{-1} (along ϵ - A_1), 0.2164 eV^{-1} (along K-H), -0.174 eV^{-1} (along M) and 0.9686 eV^{-1} (along L). Such anisotropic features were included in the present Monte Carlo approach. For the ϵ_3 valley, the effective masses along the parallel and perpendicular directions were taken to be 3.6227 and 0.2856, respectively. The nonparabolicity factors are given to be 4.4554 parallel to the c-axis and 0.22 along the perpendicular directions.

The scattering mechanisms considered were ionized impurity based on the Brooks-Herring approach, acoustic deformation potential scattering, polar-optical interactions, and intervalley deformation potential processes. The piezoelectric scattering was excluded, since it has been shown to be negligible at temperatures of 300 K and beyond. Nonequivalent intervalley scattering events were taken into account amongst all three valley types, governed by a single deformation potential and phonon energy. A 65-

Table I Parameters used in the Monte Carlo calculations for GaN

PARAMETER	VALUE
Lattice constants in meter (a , c)	3.189×10^{-10} , 5.185×10^{-10}
Dielectric constants $k(0)$, $k(4)$	9.5 , 5.35
Density (gm cm^{-3})	6.095
Acoustic velocity (ms^{-1})	4.33×10^5
Effective mass (T_1 , U - and T_3 -valley)	0.21 , 0.25 , 0.4
Valley separation (eV)	0.0 , 1.95 , 2.1
Nonparabolicity factors for the three valleys (eV^{-1})	0.19 , 0.1 , 0.0
Longitudinal optical phonon energy (eV)	0.092
Intervalley phonon energy (eV)	0.065
Acoustic deformation potential (eV)	8.0
Zero-order equivalent intervalley deformation potential (eV/cm)	0.5×10^9
Zero-order nonequivalent intervalley deformation potential (eV/cm)	1.0×10^9
First-order intervalley potential (eV)	5.0
Interface roughness correlation length (nm)	1.5
RMS fluctuations of interface roughness (nm)	0.65
Aluminum alloy fraction	x
Spontaneous polarization (C/m^2)	$-0.052 \cdot x - 0.029$
Elastic constants C_{13} and C_{33} (GPa)	$5x + 103$ and $-32x + 405$
AlGaN alloy scattering parameter (eV)	0.5

meV phonon was assumed to adequately represent both nonequivalent and equivalent intervalley scattering. A 92-meV phonon value was used for the intravalley longitudinal polar optical phonon scattering. Screening was incorporated with the random phase approximation in the long wavelength limit. The value of the inverse screening length Ξ was obtained as: $\Xi(t) = [n e^2 / k_B T_e(t)]^{0.5}$ where n is the electron density, e the electronic charge, k_B the Boltzmann constant, and T_e the effective electron temperature. This effective temperature was evaluated at each time step of the Monte Carlo simulation with the following equation:

$$T_e(t) = [2/(3k_B)] \sum_I f_I \{ 0.5 m_I \langle v^2 \rangle_I - 0.5 m_I v_{dI}^2 \} \quad (1)$$

In the above, f_I , m_I , $\langle v^2 \rangle_I$ and v_{dI}^2 refer to the electron fraction, effective mass, mean-square velocity, and drift velocity, respectively, for the I^{th} band and the index I runs over the three bands. The T_e represents an ad-hoc parameter as used by Bhapkar and Shur²⁷ and is not a real electron temperature. Pauli exclusion was included based on a rejection technique implementation first proposed by Lugli and Ferry.⁵² The material parameters required for the bulk GaN simulations were generally taken from the published literature,^{53,54} with minor adjustments.

2.2 GaN-AlGaN HEMTs

Simulations of parallel transport for the 2DEG in GaN-AlGaN HFET structures were also carried out based on the kinetic Monte Carlo approach. As is well known, mobile carriers are confined within a shallow inversion layer at the interface. Confinement then leads to the following consequences: (i) electron quantization with subband formation, leading to a two-dimensional flow; (ii) changes in the transverse wavefunctions that slightly lower the electron-phonon scattering rates, but increase the number of inter- and intra-subband processes; (iii) a relative decrease in the influence of remote ion, oxide charge, and depletion dopant ion scattering due to the increased physical separation; and (iv) the inclusion of an additional interface roughness scattering, which imparts a strong transverse electric field dependence to the channel mobility, as first shown by Sabnis and Clemens⁵⁵ for silicon. Physically, higher transverse fields

enhance the electronic confinement by drawing them closer to the interface, which leads to greater interface roughness scattering and lower mobility. The details, however, are complicated, since the relative subband occupancy and spatial electron distribution within each subband change with the transverse field by different amounts. Furthermore, as channel densities are enhanced with transverse field, free-carrier screening increases and should work to lower the effects of polar and Coulombic interactions, thereby moderating the mobility reductions.

For simplicity, it has been assumed here that the electron density within the conduction channel is uniform. Extensions to account for possible nonuniformities can be incorporated by using the procedure outlined by Ravaioli and Ferry.⁵⁶ Details of our inversion-layer Monte Carlo implementation and procedure can be found elsewhere.⁵⁷ Electron confinement was treated on the basis of a simple triangular well approximation.^{58,59} In keeping with the recent experimental work on GaN heterostructures, the *c*-axis was taken to be perpendicular to the GaN-AlGa_N interface (and hence, parallel to the growth direction), resulting in a single transverse effective mass and one set of subbands. Fang and Howard⁶⁰ variational wavefunctions were used for computations of the scattering rates. Although more sophisticated wavefunctions derived from a solution of the Poisson and Schrodinger equations could have been used, the present approach was chosen, given the existing uncertainty in the material parameters and the need to implement a relatively fast computational scheme. Besides, the variational method is known to yield reasonably accurate results and to exhibit the correct trends. A two-subband Monte Carlo model was used, that included electron interactions with acoustic modes via the deformation potential, polar optical phonon interactions, zero- and first-order intervalley deformation potential scattering,⁶¹ interface roughness,⁶² and interface ion interactions.⁵⁹ Higher subbands were ignored in the present context of low fields, as were considerations of interface phonon modes. Similarly, real-space transfer and electron flow in the AlGa_N barrier layer was also neglected. However, the role of AlGa_N on the transport was indirectly taken into account by including an alloy disorder scattering mechanism. The rationale is similar to that used by Hsu and Walukiewicz.⁶³ Screening of the polar optical and interface ion interactions was evaluated within the random phase, zero-frequency approximation⁶⁴ that requires the

evaluation of a wavevector-dependent form factor. Finally, both intra- and interband transitions were accounted for in the numerical transport simulations. Treatment of the interface roughness scattering was based on a simple Gaussian model for the autocovariance function,⁵⁹ rather than the exponential dependence used by Goodnick et al. for silicon.⁶⁵ More complicated treatments of discrete AlGa_xN islands at the interface have been suggested to include localization effects,⁶⁶ but were not used here for computational simplicity. The interface roughness scattering is most simply treated in the Born approximation by assumption that the roughness can be regarded as a weak perturbation. This is then characterized in terms of two parameters, namely, the correlation length L and root-mean-square (rms) height σ of the roughness fluctuations. This model has previously been shown to be adequate, yielding L and σ values of about 2.2 nm and 0.2 nm for silicon⁶⁷ and 2.3 nm and 0.8 nm for SiC.⁵⁷ The corresponding parameters for the GaN-AlGa_xN system, however, are not known, and have been obtained here through a best-fit procedure. Finally, degeneracy is expected to play a role in the GaN 2D system, because of the large carrier densities that have been observed experimentally. This effect, which essentially reduces the scattering rate due to a finite occupancy probability of the final state, was taken into consideration.

2.3 Polarization Effects in HEMTs

As alluded to earlier, the nitrides lack inversion symmetry and exhibit strong piezoelectric effects. Such noncentro-symmetric compounds exhibit two different sequences of their atomic layering. For GaN heterostructures with the growth direction normal to the {0001} basal plane, the atoms are arranged in bilayers. These bilayers consist of two closely spaced hexagonal layers, one formed by cations and the other by anions, leading to polar faces. Thus, a basal surface could be either Ga- (or N-) faced, corresponding to either Ga (or N) atoms on the top position of the {0001} bilayer. The two (0001) and (000 $\bar{1}$) surfaces are not equivalent, and lead to different net polarizations and internal charge densities. For clarity, an HFET with its equilibrium energy-band diagram is shown in Figs. 2(a)-2(c) for the Ga- and N-polarity. The GaN is relaxed, while the AlGa_xN has been assumed to be under tensile strain. The spontaneous polarization for AlGa_xN is larger in magnitude than that for GaN. The spontaneous and

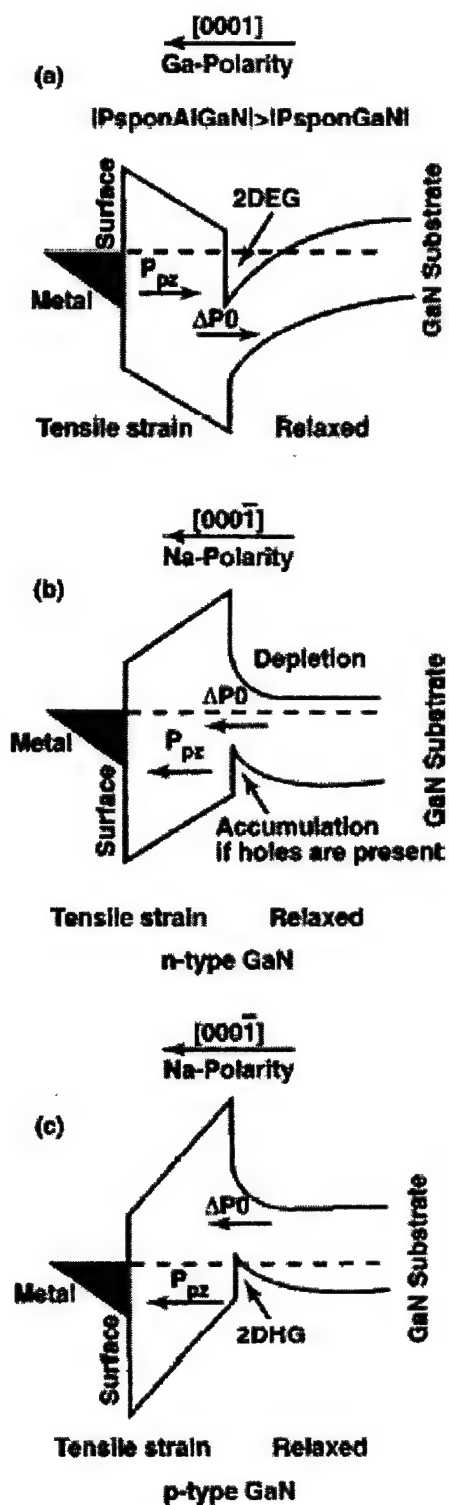


Fig. 2. Equilibrium band diagrams of a GaN-AlGaN HFET: (a) undoped GaN with Ga-polarity, (b) n-type GaN with N-polarity, and (c) p-type GaN with N-polarity.

piezoelectric polarizations support each other, and a large interface charge is created. In Fig. 2a, the resulting potential slopes toward the interface from both sides, and helps drive mobile electrons toward the channel. There is thus no specific need to dope the AlGa_N or have a spacer layer. The metallic reservoir and carrier generation processes can furnish the requisite electrons into the GaN. The situation for a N-polarity, on the other hand, is different, as shown in Figs. 2b and 2c. Both *n*- and *p*-type doping have been considered, but the net result is the same. The energy diagram predicts an accumulation of holes at the interface rather than electrons. In any case, it becomes clear that details of the surface polarity need to be taken into account, and the most effective scenario for a GaN HFET appears to be the Ga-polarity that would create a large electron pool without having to incorporate any dopant impurities.

The piezoelectric polarization P_{PE} can be calculated from the piezoelectric constants e_{33} and e_{31} as: $P_{PE} = e_{33} \epsilon_z + e_{31} (\epsilon_x + \epsilon_y)$, where ϵ_z is the strain along the *c*-axis and the in-plane strains ϵ_x and ϵ_y are equal and assumed to be isotropic. The strains can be expressed in terms of changes in the lattice constant parallel (a_o) and perpendicular (c_o) to the *c*-axis as:

$$\epsilon_x = \epsilon_y = [a(x) - a_o] / a_o , \quad (2a)$$

$$\epsilon_z = [c(x) - c_o] / c_o = -2 [C_{13}(x) / C_{33}(x)] \{ [a(x) - a_o] / a_o \} . \quad (2b)$$

In the above, $C_{13}(x)$ and $C_{33}(x)$ are the elastic constants, x is the aluminum mole fraction in the Al_xGa_{1-x}N material, and $a(x)$ is the in-plane lattice constant. Values of the piezoelectric coefficients $e_{33}(x)$ and $e_{31}(x)$, as well as the elastic constants $C_{13}(x)$ and $C_{33}(x)$ for the GaN-Al_xGa_{1-x}N system can be expressed in terms of the mole fraction x as:³⁶

$$e_{33}(x) = (0.73x + 0.73) \text{ Cm}^{-2} \quad \text{and} \quad e_{31}(x) = (-0.11x - 0.49) \text{ Cm}^{-2} , \quad (3a)$$

$$C_{33}(x) = (-32x + 405) \text{ GPa} \quad \text{and} \quad C_{13}(x) = (5x + 103) \text{ GPa} . \quad (3b)$$

Finally, the spontaneous polarization $P_{SP}(x)$ for this material system is expressed as:

$$P_{SP}(x) = (-0.052x - 0.029) \text{ Cm}^{-2} . \quad (4)$$

Hence, the magnitude of the polarization-induced interface sheet charge density $s_s(x)$ in Cm^{-2} , for an undoped, pseudomorphic, AlGa_xN-GaN single heterostructure turns out to be

$$s_s(x) = 0.0483x\{[(5x+103)/(-32x+405)](0.73x+0.73) + (0.11x+0.49)\} + 0.052x . \quad (5)$$

This interface charge works to alter the interface electric field, and hence, affects the channel density, the interface roughness scattering, the free carrier screening, and the channel degeneracy. The channel electron charge density $qn_s(x)$, is then :

$$qn_s(x) = s_s(x) - [\epsilon_0 \epsilon(x)/d] \{N_b(x) + E_F(x) - \chi\} E_c(x) , \quad (6)$$

with ϵ_0 being the permittivity of free space, $\epsilon(x)$ the dielectric constant, d the Al_xGa_{1-x}N barrier thickness, $N_b(x)$ the Schottky-barrier height, $E_F(x)$ the Fermi level with respect to the GaN conduction band-edge, and χ the conduction band offset. Using values reported in the literature,^{68,69} leads to :

$$\epsilon(x) = -0.5x + 9.5 , \quad (7a)$$

$$N_b(x) = (1.3x + 0.84) , \quad (7b)$$

$$\chi E_c(x) = 0.7 [E_G(x) - E_G(0)] , \quad \text{and} \quad (7c)$$

$$E_F(x) = \{[9B\Sigma q^2 n_s(x)]/[8\epsilon_0 \epsilon(x) \{8m^*(x)\}^{0.5}]\}^{2/3} + [B\Sigma^2 n_s(x)]/m^*(x) . \quad (7d)$$

The effective mass $m^*(x) \sim 0.22 \times 9.1 \times 10^{-31} \text{ Kg}$,⁷⁰ while the energy gap $E_G(x)$ is measured in eV to be⁷¹ :

$$E_G(x) = 6.13x + 3.42(1-x) - x(1-x) . \quad (7e).$$

3. GaN HEMTs -- ROLE OF DISLOCATIONS

Epitaxial layers of GaN can contain a high density of dislocations, which form because of the absence of a suitably lattice-matched substrate for growth. Both sapphire

and silicon carbide substrates have such problems. These dislocations are predominantly oriented parallel to the c axis of the material.⁷² Dislocations densities in GaN layers grown on sapphire or SiC substrates range between 10^8 – 10^9 cm⁻².⁷³ One of the important effects of dislocations that have been reported in the GaN arena is on carrier scattering⁷⁴⁻⁷⁵ due to the creation of localized charge centers. For example, room temperature electron mobilities were shown to decrease from about 600 cm²/Vs to 150 cm²/Vs as the dislocation density increased from 4×10^8 to 2×10^{10} cm⁻² in bulk GaN films.⁷⁶ Using a Boltzmann transport model with dislocation scattering treated in terms of a screened interaction between mobile electrons and line-charges, Look and Sizelove⁷⁷ were able to fit the bulk GaN mobility data rather well. The electron mobility vs density was shown to have a local maxima and *decrease* with density at low concentrations, due to reductions in the screening of dislocation scattering. Another unusual transport phenomena in bulk GaN, attributed to dislocations, was that of a mobility collapse at low carrier densities.⁷⁸ In a theoretical analysis,⁷⁹ it was shown that this sharp density dependent transition between regions of low- and high-mobilities could arise from a collective effect of dislocation walls leading to the formation of internal potential barriers. Thus, the role of dislocations on the transport in bulk GaN appears to be well recognized and shown to have a strong impact on carrier mobilities.

By contrast, the role of dislocations on the transport of a two-dimensional electron gas (2DEG) has not been studied in detail. Some reports of carrier mobilities in high electron mobility transistors (HEMTs) indicate that dislocation scattering may not play such a significant role.⁸⁰ This suggests that the role of screening, which is known to be somewhat different in two-dimensional systems, might not be quite as strong. Part of the resolution may also lie in the details of the mobility data. For instance, the mobility values at 300 Kelvin were shown to decrease only mildly, with variations in the 2DEG concentration. The mobility was reported to vary from about 1550 cm²/Vs to 1000 cm²/Vs.⁸⁰ The range of densities for these cases, however, was roughly around 10^{13} cm⁻², and hence, fairly large on an absolute scale. By comparison, channel densities in the well-known GaAs-heterostructure systems, are seldom as high as 10^{13} cm⁻². Screening, which might be responsible for such mobility effects, is quantitatively quite complicated in a multi-subband 2D system. Its evaluation, even in the random phase approximation

(RPA), requires an inversion of a dielectric matrix.⁸¹ For the simplest situation of single subband static screening under the RPA and in the long-wavelength limit, the dielectric function can be characterized by a wavevector independent inverse screening length Ξ . This inverse screening length is independent of the carrier density at low temperatures⁸², and proportional to the 2DEG concentration under non-degenerate conditions.⁸³ Expressions for Ξ under these two limiting conditions are:

$$\Xi (\text{low temperature}) \sim \{ m^* e^2 \} / [B \Sigma^2 (\epsilon_1 + \epsilon_2)] \quad , \quad (8a)$$

$$\text{and } \Xi (\text{non-degenerate}) \sim [n_{2D} e^2] / [(\epsilon_1 + \epsilon_2) k_B T] \quad , \quad (8b)$$

where, ϵ_1 and ϵ_2 are the AlGaIn and GaN material permittivities, m^* the effective electronic mass, n_{2D} the 2DEG density, k_B the Boltzmann constant, and T the temperature in Kelvin.

Clearly, at low electron concentrations, and/or high temperature operation as would practically occur for GaN HEMTs, eqn. (8b) would be more appropriate. In the GaN-based experimental devices, however, the 2DEG density was relatively high. Hence, the screening length would only have been weakly dependent on the 2DEG density. This might have been a factor in the apparent lack of a strong density dependent affect on the mobility. Besides, for the room temperature experiments, phonon-scattering may be the dominant interaction, and would then overwhelm the role of other mechanisms such as dislocation scattering. A more appropriate situation for probing the impact of dislocations on 2DEG carrier transport would be at low densities. Moderate-to-high operating temperatures might not be constructive, as the phonon scattering would increasingly dominate. The inverse screening at low carrier densities would be reduced, and collective effects brought about by dislocations (such as localized strain and charges at the hetero-interface) could prevail. Such a low-density scenario is not completely hypothetical, since low concentrations from a practical standpoint, would arise for thinner AlGaIn barrier layers,⁸⁴ devices with lower Al mole fractions,⁸⁴ or during the negative polarity excursions of the gate voltage for ac operation.

Traditional evaluations of electronic transport in the presence of defects, have considered Coulomb interactions between mobile carriers and dislocation charges.⁸⁵ The

strain fields associated with defects have generally been neglected. However, recent calculations show that no internal electric fields are generated for screw dislocations, and that for edge dislocations, polarization charge density and electric fields are generated only in the *near interfaces*.⁷³ This makes the dislocation scattering especially important and germane to interface transport, as in the case of a two-dimensional electron gas (2DEG) in HEMTs. In a very recent report, the effect of such edge-dislocation induced strain fields on 2DEG scattering was analyzed to obtain an expression for the strain-limited mobility.⁸⁶ A useful closed-form expression for dislocation mobility was presented, though the results relied on the relaxation time approximation, and collective contributions of other scattering mechanisms (e.g. carrier-phonon) were not taken into account. In any case, it was shown that for a given dislocation density, the mobility reduction would be the largest at the smallest carrier density n_{2D} .

As is rapidly becoming clear, the 2DEG density n_{2D} is controlled by several factors such as the thickness of the AlGaIn barrier layer, the presence of surface states and role of possible capping layers.^{87,88} Hence, an explicit connection with the structure and/or geometry of the HEMT device exists.⁸⁴ Fig. 3 shows an energy band schematic for a GaN-AlGaIn HEMT with a GaN cap layer. In general, the capping layer shown may be of another material (e.g. silicon nitride) or might even be totally absent.

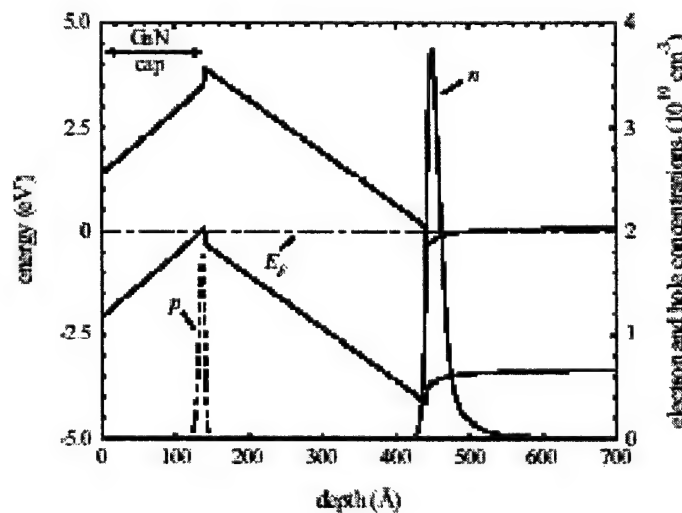


Fig. 3. Energy band schematic for a GaN HEMT with an AlGaIn barrier layer and a GaN capping layer. The surface potential is assumed fixed with negligible doping in AlGaIn.

Regardless of the details, the 2DEG density depends on the AlGaN barrier doping and the position in energy of the interface donor-like states above the Fermi level. The latter is controlled by the barrier and capping layer thicknesses.⁸⁴ It is, therefore, possible to have situations (e.g. HEMTs with barriers having no intentional doping, but with a capping layer) where n_{2D} might be low, with holes present at the AlGaN-GaN cap interface. It would also be possible to *lower* the inversion charge upon the application of a positive gate potential, with the holes moving out towards the 2DEG at the GaN-AlGaN interface. This has obvious implications for large signal behavior of HEMTs, with regards to signal distortion and intermodulation.⁸⁹

Situations of low n_{2D} coupled with the possibility of strain-fields (and concomitant local shifts in the energy band), can lead to : (i) Increased localization of charge within the 2DEG, (ii) Spatially non-uniform screening., and (iii) Scattering enhancement of the 2DEG. Under such a scenario, electrons would be bunched within pockets of energy minima. Electron flow would then be affected by the Coulomb repulsion from charge localized at dislocations, leading to disruption in directed motion and lower mobilities. A rigorous treatment of such transport conditions would need the inclusion of quantization effects within the regions of localized strain, and use of a Molecular Dynamics (MD) approach⁹⁰. However, neither has been applied here in our calculations, for the following reasons. The maximum shift $\ast V$ in the conduction band is given by: $\ast V \sim a_c b (2Br)^{-1} [(1-2\epsilon)/(1-\epsilon)]$, where b is the Burgers vector, (ϵ the Poisson's ratio, and a_c the band deformation potential. Using typical values, $b = 3.189 \text{ \AA}$, ($\epsilon = 0.3$, and $a_c = -8 \text{ eV}$), leads to a maximum radial distance $r_{\max} = 8.9 \text{ nm}$, at which the $\ast V$ magnitude equals the room temperature thermal energy. Hence, it is expected that carrier at distances larger than r_{\max} would not be localized at the dislocations, and would remain largely unaffected. Since, this r_{\max} value is much smaller than the typical length scales (e.g. either the adjacent dislocation distances of $\sim 300 \text{ nm}$, or the typical HEMT dimensions), such quantization effects and perturbations in local density were ignored. Our reason for not using the MD approach was to avoid computational complexity. Besides, MD has an advantage primarily in situations that involve high electron and/or dislocation concentrations. However, the focus here is on low electron densities for which screening and effective mobilities are the smallest. It is also assumed that

collective dislocation effects would not be an issue due to improvements in processing capability.

Dislocation scattering was treated based on deformation potential interaction of electrons from the strain fields surrounding edge dislocations. The effect of a strain in the quantum well is to shift the conduction and valence band edges. Such shifts in the conduction band edge have been calculated,⁹¹ and the perturbing potential $*V$ for electron scattering can be shown to be :

$$|*V(r,2)| = \{ a_c b / (2Br) \} [(1-2\cos(2\theta)/(1-\cos(2\theta))) \sin(2\theta)], \quad (9)$$

where 2θ the polar angle with respect to the Burgers vector in the 2D plane. A simple result for the dislocation scattering rate can be obtained if the electronic states in the GaN channel are assumed to be strictly two-dimensional in nature. For this case, the wavefunctions $P_i(r)$ for the i^{th} subband are expressed as: $P_i(r) = S^{-1/2} \exp(ik \cdot r)$ with r and k being the position and wavevectors parallel to the interface, and S the surface area. The matrix element $M_{ij} = \langle P_i | *V(r,2) | P_j \rangle$ then is:

$$\langle P_i | *V(r,2) | P_j \rangle = |*V(q,N)| = \{ a_c b / (Sq) \} [(1-2\cos(N)/(1-\cos(N))) \sin(N)], \quad (10)$$

where N is the angle between the Burgers vector and q the wavevector magnitude between the initial state (k_i) and final in-plane state (k_f). Thus, $q = |k_f - k_i|$. Use of the Fermi's Golden-rule for this two-dimensional case, with an additional screening factor of $k(q) [= 1 + \Xi/q]$ for the matrix element (10), then leads to the following energy-dependent scattering rate $S_{\text{dis}}(E)$ for parabolic bands:

$$S_{\text{dis}}(E) = \{ N_{\text{dis}} a_c^2 b^2 [(1-2\cos(N)/(1-\cos(N)))^2] [4B\Sigma E]^{-1} \int_0^1 du [\{u + 0.5\Sigma\Xi/(2m^*E)\}^{0.5} (1-u^2)^{0.5}]^{-1} \}, \quad (11)$$

where N_{dis} is the dislocation density, m^* the electron effective mass, and Ξ the inverse screening length. In the above, an average over the angles N [defined in (10)] has been set to $1/2$ on the assumption that the Burgers vectors associated with the various

dislocations are randomly oriented. For purposes of a Monte Carlo implementation, the final in-plane angle after a dislocation scattering event needs to be determined. This is easily done based on the associated angular probability distribution $p(2)$. In this case, from (11) :

$$p(2) = [(2 / \Sigma) \{2m^*E\}^{0.5} \sin(2/2) + \Xi]^{-2} . \quad (12)$$

Hence, for the j^{th} scattering event, the requisite scattering angle 2_j can be obtained by generating a random number r_j ($0 \leq r_j < 1$), and using the above $p(2)$ as:

$$r_j = [\int_0^{2_j} p(2) d2] / [\int_0^{2B} p(2) d2] . \quad (13)$$

Due to the strict 2D nature of the carrier confinement assumed for the above, analysis, the scattering rate is independent of the sub-band index. A more accurate result can be obtained by allowing for the inclusion of the envelope function along the perpendicular z -direction. Using the following separable form⁹²: $P_i(\mathbf{r}) = S^{-1} \exp(i\mathbf{k} \cdot \mathbf{r}) F_i(z)$, leads to:

$$|*V(q,N)| = \{a_c b / S\} [(1-2\alpha)/(1-\alpha)] \sin(N\alpha) \int_0^L F_j^*(z) F_i(z) dz \int_0^L r J_1(qr) / [r^2 + z^2]^{0.5} dr , \quad (14)$$

where $J(x)$ is the Bessel function. Integration over dr yields:

$$|*V(q,N)| = \{a_c b / S\} [(1-2\alpha)/(1-\alpha)] \sin(N\alpha) \int_0^L F_j^*(z) F_i(z) \times [I_0(x) K_1(x) - I_1(x) K_0(x)] dz, \quad (15)$$

where $x = qz/2$, the $I_i(x)$ and $K_i(x)$ are Bessels functions of imaginary argument. For the two lowest subbands, the following expressions for the envelope wavefunctions result⁹²:

$$F_1(z) \sim [b_0^3/2]^{0.5} z \exp(-b_0 z/2) , \quad (16a)$$

$$\text{and, } F_2(z) \sim [3b_1^5 / \{2(b_0^2 - b_0 b_1 + b_1^2)\}]^{0.5} [z - \{(b_0 + b_1)/6\} z^2] \exp(-b_1 z/2) , \quad (16b)$$

with fixed parameters b_0 and b_1 that depend on the doping and channel densities, barrier thickness etc.. As such, the integral in (16) can only be evaluated through a numerical procedure. However, useful analytical expressions can be obtained by recognizing that the functions $F_i(z)$ fall off rapidly with the distance, and hence, the Bessel functions $I_i(x)$ and $K_i(x)$ can be approximated for small x . Using simple polynomial expressions for $I_i(x)$ and $K_i(x)$ ⁹³, and employing the result for the matrix element in the evaluation of the Fermi golden-rule scattering rate, leads to the following intra-subband dislocation scattering result :

$$S_{dis}^{11}(E) \sim N_{dis} a_c^2 b^2 [(1-2Q)/(1-Q)]^2 [4B\Sigma E]^{-1} \int_0^1 du F[\{u + .5\Sigma\Xi/(2m^*E)^{0.5}\}(1-u^2)^{0.5}]^{-1} du . \quad (17)$$

Eqn. (17) is almost identical to (11), except for the additional energy dependent factor $F(E)$ given as: $F(E) = (1 + 84.3 m^* E u^2 / \{\Sigma b_0\}^2)$. For small energies, the 2D and quasi-2D scattering rate expressions match. The increase in scattering with energy is associated with the larger changes in wavevector q . The angular probability function, required for selecting the final state after dislocation scattering in a Monte Carlo implementation, is modified because of the $F(E)$ factor. Instead of (12), the angular function becomes:

$$p^{11}(2) = \{1 + 84.3 m^* E \sin^2(2/2) / (\Sigma b_0)^2\} [(2 / \Sigma) \{2m^* E\}^{0.5} \sin(2/2) + \Xi]^{-2} . \quad (18)$$

The intra-subband scattering rate $S_{dis}^{22}(E)$ can also be obtained by using the $F_2(z)$ wavefunctions. The rate for the intra-subband transition $2 \rightarrow 2$ is similar in form to $S_{dis}^{11}(E)$, except for a different $F(E)$ factor. Denoting this factors as $F^{22}(E)$, one obtains:

$$F^{22}(E) \sim A (b_0/b_1 - 36.1468 m^* E u^2 / \{\Sigma b_1\}^2) , \quad (19)$$

where $A = [9b_1^4 / \{(b_0^2 - b_0 b_1 + b_1^2)^2\}]$. The angular function $p^{22}(2)$ is:

$$p^{22}(2) = \{b_0/b_1 - 36.1468 m^* E \sin^2(2/2) / (\Sigma b_1)^2\} [(2 / \Sigma) \{2m^* E\}^{0.5} \sin(2/2) + \Xi]^{-2} . \quad (20)$$

The inter-subband rates $S_{\text{dis}}^{12}(E)$ and $S_{\text{dis}}^{21}(E)$ are equal, but very small in comparison due to minimal overlap. Hence, these have been ignored here. In any case, the dislocation scattering rate depends on the b_0 and b_1 parameters. These are influenced by the electric field at the GaN-AlGa_N interface. Hence, it becomes clear that the dislocation scattering contributions to carrier mobility should exhibit a dependence on both the Aluminum mole fraction and barrier thickness as these affect the interface electric field.

Computations of the intra- and inter-subband scattering rates require evaluations of the b_0 and b_1 parameters. Approximate solutions can be obtained on the basis of the energy minimization principle.⁹² However, a slightly different approach was used here. A numerical procedure based on a self-consistent solution of the Schrödinger, Poisson, and charge balance equations was employed to obtain the eigen-functions explicitly. The resulting wavefunctions were then used to extract the b_0 and b_1 parameters. Details of this method for the GaN electronic system, with more recent inclusions of the hole states, have been reported elsewhere.⁹⁴⁻⁹⁵ Briefly, both spontaneous and piezoelectric polarizations and exchange-correlation corrections to the Coulomb interaction are included in the calculation of the electrostatic potential. Strain is included in the eigenstate calculation via deformation potential theory. The large band gap of the host materials enables the ϵ_{7c} conduction band to be decoupled from the ϵ_{9v} and two ϵ_{7v} valence bands. The result is that the standard $8 \times 8 \mathbf{k} \cdot \mathbf{p}$ Hamiltonian in an $s - p$ basis is transformed into two equivalent 1×1 Hamiltonians for the ϵ_{7c} conduction bands and a 6×6 Hamiltonian for the A , B , and C valence bands. The electron eigenstates are calculated by solving the one-band Schrödinger equation across a c -axis slice of the HFET. The hole eigenstates are calculated along the same axis using a $6 \times 6 \mathbf{k} \cdot \mathbf{p}$ method. The complete electron distribution was calculated by summing the individual contributions from about 25 electron subbands. Summations for the hole distribution were performed over 70 hole subbands each containing an admixture of ϵ_{9v} and ϵ_{7v} states. Also, surface states were included using Fermi-Dirac statistics, since surface donors strongly influence the 2DEG density and explains the experimental data quite well. The resulting model allows for the calculation of electron eigenfunctions, energies and the free electron distributions as a function of the AlGa_N barrier thickness and alloy composition.

Fig. 4 shows the scattering rate as a function of energy with Ξ as the variable parameter. For calculations, the dislocation density was $2 \times 10^9 \text{ cm}^{-2}$. Since the scattering

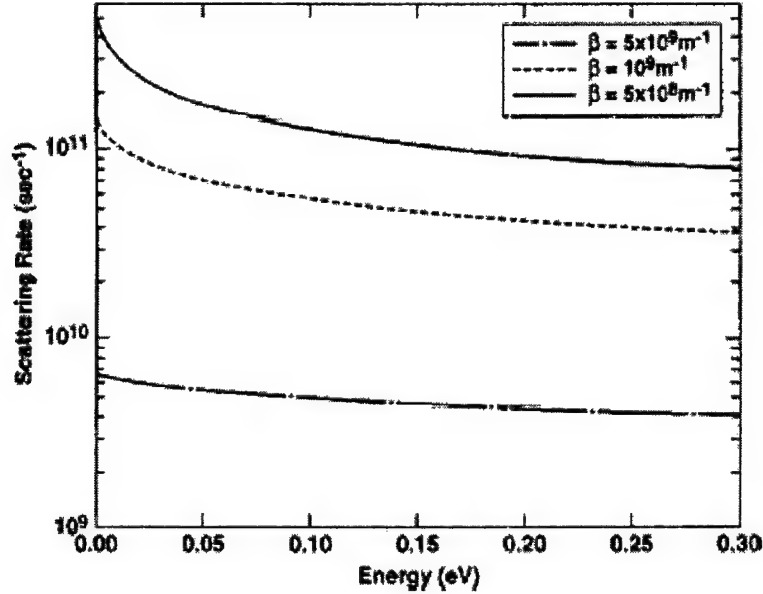


Fig. 4. Energy dependent dislocation scattering at 300 K with the inverse screening length as the parameter. A dislocation density of $2 \times 10^9 \text{ cm}^{-2}$ was used.

is largest at small energies, one can expect the impact to be strongest on carrier mobility, rather than the high-field drift velocity. Also, the effects would be greater at low q_s , and hence, for situations in which the average density of mobile electrons in the channel was low. High defect densities (which might trap free electrons), or application of a positive gate bias both provide such conditions. For HEMTs with a capping layer above the AlGaIn barrier, a positive bias would drive holes from the capping layer-AlGaIn interface towards the 2DEG. For situations in which the capping layer was absent, the positive voltage would lower the surface states in energy space, increase their occupancy and thereby, lower n_{2D} .

4. INTERMODULATION DISTORTION ANALYSIS

Mathematical evaluation of the nonlinear characteristics of field effect transistors (FETs) has often been based on the Volterra-Wiener formalism.^{96,97} However, this

technique is only applicable to small-signal inputs, and it neglects memory-effects. A more appropriate scheme for an analytical solution would be a polynomial representation of the device output current (or current density J_0) as a function of the input gate voltage V_G .⁹⁸ Thus, $J_0(V_G) = K_0 + K_1 V_G + K_2 V_G^2 + K_3 V_G^3 + \dots$ with the coefficients K_i being some constants. For accurate and realistic results, the coefficient can either be extracted from actual experimental data, or from curve-fitting to Monte Carlo predictions of the current response. For a single sinusoidal input, $V_G(t) = A \cos(Tt)$, the polynomial representation yields the following current density function to fifth order:

$$\begin{aligned} J_0(A,t) = & (1/2)K_2A^2 + (3/8)K_4A^4 + \{K_1A + (3/4)K_3A^3 + (5/8)K_5A^5\} \cos(Tt) + \\ & + \{(1/2)K_2A^2 + (1/2)K_4A^4\} \cos(2Tt) + \{(1/4)K_3A^3 + (5/16)K_5A^5\} \cos(3Tt) + \quad (21) \\ & + \{(1/8)K_4A^4\} \cos(4Tt) + \{(1/16)K_5A^5\} \cos(5Tt) . \end{aligned}$$

For a two-tone input gate signal $V_G(t) = A \cos(T_1t) + A \cos(T_2t)$, the current density terms at the fundamental and intermediate frequencies based on a fifth order polynomial are:

$$\begin{aligned} J_0(A,t) = & \{K_1 + (9/4)K_3A^3 + (25/4)K_5A^5\} [\cos(T_1t) + \cos(T_2t)] + \\ & + \{(3/4)K_3A^3 + (25/8)K_5A^5\} [\cos\{(2T_1 - T_2)t\} + \cos\{(2T_2 - T_1)t\}] + \dots + \quad (22) \end{aligned}$$

The choice to fifth order is meant to represent an acceptable tradeoff between increasing accuracy with the inclusion of higher orders at the expense of enhanced computational complexity. Based on the above, expressions for the input power (P_i), the output power (P_o), in dBm units, at the fundamental frequency can be obtained. These are:

$$P_i = 10 \log_{10} [A^2 10^3 / (2R_i)] \sim 30 + 10 \log_{10} [A^2] , \quad (23)$$

and,

$$\begin{aligned} P_o = & 10 \log_{10} [\{K_1A + (3/4)K_3A^3 + (5/8)K_5A^5\}^2 10^3 / (2R_o)] \\ \sim & 30 + 10 \log_{10} [\{K_1A + (3/4)K_3A^3 + (5/8)K_5A^5\}^2] , \quad (24) \end{aligned}$$

where R_i and R_o are the respective input and output resistances. Similarly, the variation of the third-order intermodulation power P_{IP} , in dBm, with the gate signal amplitude “A” is :

$$P_{IP} \sim 30 + 10 \log_{10} \left[\left\{ (3/4)K_3A^3 + (25/8)K_5A^5 \right\}^2 \right] . \quad (25)$$

Based on the above equations, the input-output power curves can be obtained, provided the coefficients K_i are given or can be extracted.

The above approach, though reasonable, excludes memory effects within the system. It is implicit that the output changes instantaneously in response to the fluctuations of the input signal. A more realistic representation is provided through Monte Carlo simulations that can yield an output current due to a collective motion of the 2DEG ensemble in response to gate voltage variations. The history of individual particles is automatically included, as are all details of scattering that control the dynamical evolution of the carriers. The non-Markovian behavior is expected to become important for short devices and/or high operating frequencies. Here, both the analytical results and the Monte Carlo calculations have been used to probe the IMD behavior.

5. ANALYTICAL MODEL FOR INTERMODULATION DISTORTION

A more appropriate and simpler scheme for evaluation would be through an analytical solution would be a polynomial representation of the device output current (or current density J_0) as a function of the input gate voltage V_G .^{97,98} Thus, $J_0(V_D, V_G) = n_s(V_D, V_G) q v(V_D, V_G)$, where n_s is the inversion charge density and $v(V_D, V_G)$ the effective drift velocity.

For all practical purposes, the density of inversion electrons in the GaN channel is well above 10^{16} m^{-2} level. This has also been verified through the calculations presented later in this report. At these high densities, equation (7d) can roughly be linearized and expressed in the form: $E_F(x) = A(x) n_s(x)$. Combining equations (7) and using the linearized expression for $E_F(x)$, yields the following inversion charge density relation:

$$n_s(x, y) = \frac{\epsilon_s(x)}{[0, (x)/d]} \{ N_b(x) + E_F(x) - E_c(x) - V_G + V(y) \} , \quad (26a)$$

$$\text{i.e. } n_s(x,y) \cong B_1(x,V_G) - B_2(x) V(y) - [_{,0}(x)/d] A(x) n_s(x), \quad (26b)$$

$$\text{where, } B_1(x,V_G) = B_{10}(x) + [_{,0}(x)/d] V_G ; \quad B_2(x) = [_{,0}(x)/d] \quad (26c)$$

$$\text{and , } B_{10}(x) = s_s(x) - [_{,0}(x)/d] \{N_b(x) - \} E_c(x) \} . \quad (26d)$$

Hence, more compactly :

$$n_s(x,y) = [B_{10}(x) + \{_{,0}(x)/d\} V_G - B_2(x) V(y)] / \{1 + [_{,0}(x)/d] A(x) \} , \quad (26e)$$

which can be used in the evaluation of device current.

The drift velocity term $v(V_D, V_G)$ is more difficult to model analytically. Perhaps, the best approach to an analytical expression for the drift velocity is to first obtain velocity-field characteristics based on a rigorous Monte Carlo-type simulation. These curves can then be fit to polynomials with V_D and V_G as the independent parameters. Unfortunately, the use of such polynomials precludes a closed-form analytical expression for the device current-voltage characteristics. For example, the following functional form has commonly been employed for the velocity-field (v - E) curve:

$$v(E) = [\mu E + v_{sat} (E/E_c)^n] / [1 + (E/E_c)^n] , \quad (27a)$$

where μ is the low-field mobility, v_{sat} the saturation velocity, E_c the electric field corresponding to the peak velocity, and n an exponent usually equaling about 4. The above form includes both a velocity overshoot behavior and high-field saturation. Using (26e) and (27a) for the charge density and velocity, respectively, then yields the following expression for the source-drain current I_{DS} :

$$I_{DS} = Zq \{ [B_1(x,V_G) - B_2(x) V(y)] / \{1 + [_{,0}(x)/d] A(x)\} \} [\mu E + v_{sat} (E/E_c)^n] / [1 + (E/E_c)^n] , \quad (27b)$$

where Z is the device transverse dimension, and q the electronic charge. Using $E = dV(y)/dy$, equation (27b) can be set up as an integral equation. However, an analytical

solution cannot be obtained, and so a closed-form current-voltage (I_{DS} - V_D) relationship in terms of V_G does not result.

This difficulty can be overcome by using a slightly simpler (and more approximate) expression for the v - E curve, as first suggested by Trofimenkoff⁹⁹. A closed form relation can then be obtained. The Trofimenkoff expression is :

$$v(E) = \mu E / [1 + (\mu/v_{sat}) E] \quad , \quad (28)$$

where μ is the low-field mobility, and v_{sat} the saturation velocity. Though equation (28) does successfully represent a low-field mobility and a high-field saturating behavior, it does not mimic the velocity overshoot characteristic. Hence, strictly the Trofimenkoff expression is mostly directly applicable to semiconductors such as Silicon. In the present context of AlGaIn-GaN HEMTs, the above velocity-field model can perhaps still be used as a simple and adequate representation, at least at low drain voltages. Furthermore, previous Monte Carlo simulations for the GaN HEMTs have shown an absence of velocity overshoot⁴¹. Physically, this can be the result of real space transfer of electrons from the GaN channel into the bulk AlGaIn region. The higher electronic mass in AlGaIn reduces the effective electronic drift velocity, and effectively suppresses the overshoot phenomena. A necessary condition for this is that the Γ -L valley separation be greater than the GaN-AlGaIn conduction band offset energy. This condition is easily met for the GaN HEMT system at the mole fractions typically used, and so the velocity overshoot is strongly curtailed. Consequently, the use of the simpler Trofimenkoff velocity-field expression becomes justifiable.

Using equation (28), the current equation can be cast in the following form:

$$I_{DS} = Zq [\{B_1(x, V_G) - B_2(x) V(y)\} / \{1 + [\mu_0(x)/d] A(x)\}] [\{\mu dV(y)/dy\} / \{1 + (\mu/v_{sat}) dV(y)/dy\}] \quad . \quad (29)$$

Integrating the above between $y = 0$ and $y = L$, corresponding to voltages $V(0) = 0$ and $V(L) = V_D$, one obtains the following current-voltage characteristics:

$$I_{DS} = \{ \mu Z q V_D [B_{10}(x) + \{ \rho_0(x)/d \} V_G - 0.5 B_2(x) V_D] \} / [L + (\mu/v_{sat}) V_D] \quad (30)$$

In reality, the velocity $v(E)$ is not controlled by the channel electric field E alone, as suggested by eqn. (28). Instead, it is also influenced by the gate bias V_G for a variety of reasons. First, V_G controlled 2DEG density variations affect carrier scattering through changes in the screening of polar interactions and degeneracy modification.⁴¹ Next, with increasing gate bias, interface roughness scattering can change nonlinearly with transverse electric field. This would lower the velocity with increasing V_G . The degree of real space transfer of electrons from GaN into the AlGaN layer is also dependent on V_G . Such a gate voltage influence on the channel drift velocity can, therefore, be better represented by modifying the v - E expression (28) to include V_G as a controlling parameter. Consequently, the mobility and saturation velocities would not be constants, but rather become gate voltage dependent fitting parameters, modifying the velocity-field relation (28) as:

$$v(E, V_G) = E K_1\{V_G\} / [1 + E K_2\{V_G\}] \quad (31)$$

In the above, $K_1\{V_G\}$ and $K_2\{V_G\}$ represent V_G dependent mobility and an inverse effective field, which can, in principle, be extracted from a curve fitting procedure to the results of Monte Carlo simulations at various gate voltages. More generally, of course, $K_{1,2}\{V_G\} / K_{1,2}\{V_G, T\}$ since the mobility and saturation velocity are functions of the operating temperature T as well. Use of (31) instead of (28), modifies the $I_{DS} - V_D$ characteristics to the following form:

$$I_{DS} = (K_1\{V_G\} Z q V_D [B_1(x, V_G) - 0.5 B_2(x) V_D]) / [L + K_2 V_D] \quad (32)$$

In the above, the $B_1(x, V_G)$ term depends linearly on gate voltage. The non-linearity arises from the $(K_1\{V_G\}/[L + V_D K_2\{V_G\}])$ factor and depends on the device length L , the drain bias V_D , operating temperature and Aluminum mole fraction. Denoting this factor, for convenience, in terms of a polynomial in V_G with coefficients $C_i(V_D)$ as:

$$K_1\{V_G\}/[L + V_D K_2\{V_G\}] / C_0(V_D) + C_1(V_D) V_G + C_2(V_D) V_G^2 + C_3(V_D) V_G^3 + \dots , \quad (33)$$

the various frequency components of I_{DS} can be obtained for sinusoidal gate inputs. For a large signal, constant amplitude, gate voltage $V_G = A \cos(\omega t)$, the intrinsic device current at the fundamental frequency to lowest order would be:

$$I_{DS} \simeq AZqV_D [C_1 \{B_{10}(x) - 0.5 B_2(x)V_D\} + (C_0 + 0.75C_2A^2) B_2(x)] \cos(\omega t) , \quad (34a)$$

$$\text{i.e. } I_{DS}(\omega) / I(x, V_D) \cos(\omega t) . \quad (34b)$$

Based on the above, the input power (P_i) and output power (P_o) in dBm units become: $P_i = 10 \log_{10} [A^2 10^3/(2R_i)]$ and $P_o = 10 \log_{10} [I^2(x, V_D) 10^3/(2R_o)]$ for input and output resistance R_i and R_o . Thus, depending on the sign of the coefficients C_0 , C_1 and C_2 , there could either be gain enhancement or compression.

Inter-modulation distortion characteristics naturally result by considering a two-tone gate input signal $V_G(t) = A \cos(T_1t) + A \cos(T_2t)$. Based on (23) and (24), device current at the intermediate frequencies $|2T_{1,2} - T_{2,1}|$ to lowest order is given as:

$$I_{DS} \simeq 0.75A^3 ZqV_D [C_3\{B_{10}(x) - 0.5B_2(x)V_D\} + C_2 B_2(x)] [\cos\{(2T_1 - T_2)t\} + \cos\{(2T_2 - T_1)t\}] \quad (35)$$

The corresponding inter-modulation power P_{IMD} is:

$$P_{IMD} = 10 \log_{10} [(0.75A^3 ZqV_D [C_3\{B_{10}(x) - 0.5B_2(x)V_D\} + C_2 B_2(x)])^2 10^3/(2R_o)] . \quad (36)$$

The third-order intercept point (IP_3) can be obtained from (34) and (36) since it is defined to be the power level at which the linear extrapolation of P_o equals the IMD power. In this case, P_{IP_3} equals:

$$P_{IP_3} = 10 \log_{10} [\{4/3\} (ZqV_D)^2 \{T_1(x)^3 / T_2(x)\} \{10^3/(2R_o)\}] , \quad (37a)$$

$$\text{where, } T_1(x) = C_1\{B_{10}(x) - 0.5 B_2(x) V_D\} + C_0 B_2(x) , \quad (37b)$$

$$\text{and, } T_2(x) = C_3\{B_{10}(x) - 0.5 B_2(x) V_D\} + C_2 B_2(x) . \quad (37c)$$

6. RESULTS AND DISCUSSION

6.1 Transport Calculations For Bulk GaN

Results of the Monte Carlo simulation for bulk wurtzite GaN at 300 K are given and discussed first. Some of the transport parameters for GaN material have not explicitly been measured. Hence, as a first step, the 10,000-electron Monte Carlo code was used without any quantization effects to simulate the transport in bulk material. The primary objective was to start with as many of the known parameters for wurtzite GaN as possible, and fine tune other values to achieve a reasonable fit with available reports in the literature. Figure 5 shows the transient drift velocity of the electronic ensemble in bulk GaN for different values of the electric field parameter. An upperbound of 400 kV/cm was chosen to prevent the electronic energies from becoming excessively large. This precaution was necessary, since the present simulation does not include a full bandstructure calculation, but instead relies on a simple nonparabolic approach to the energy bands. A velocity overshoot arising from intervalley transfer is immediately seen

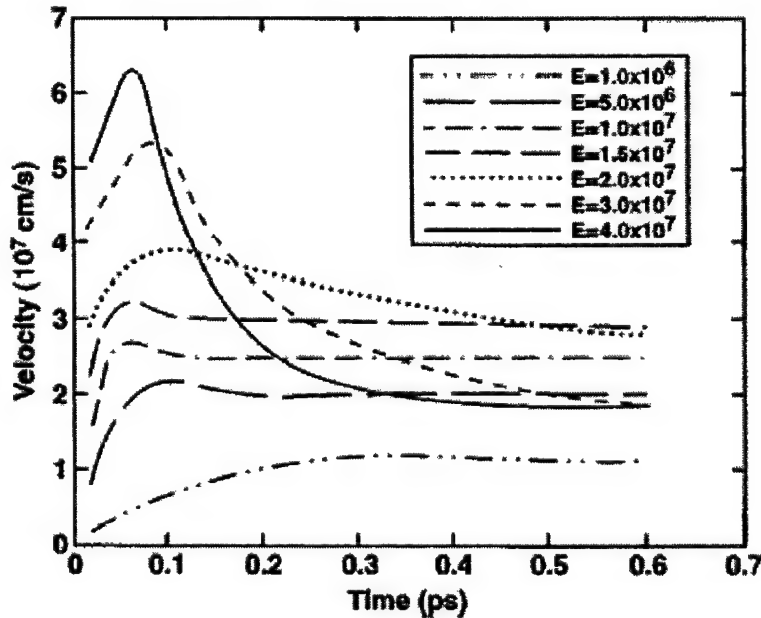


Fig. 5. Monte Carlo results of the transient electron drift velocity at 300 K in wurtzite GaN for different fields.

from the curves, similar to the occurrence for GaAs. The threshold field for this transferred electron effect is predicted to be around 170 kV/cm. For electric fields higher than this threshold, there is a monotonic decrease in the steady-state drift velocity, although a much higher transient overshoot results. At 400 kV/cm, for example, a peak velocity of about 6.5×10^7 cm/s is predicted. The central conclusion is that GaN material can be well utilized for nonequilibrium transport and would yield fast response for scaled-down structures. Steady-state values at the high fields are also larger than those obtainable for GaAs. The field-dependent velocity-field curves for the material at two different temperatures are shown in Fig. 6. A fairly large drift velocity of 1.4×10^7 cm/s

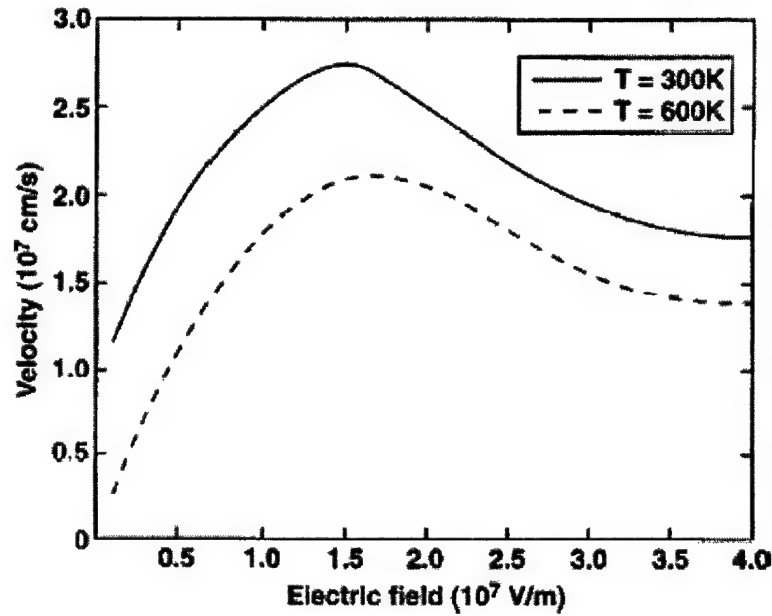


Fig. 6. Monte Carlo results of the electron velocity-field characteristics at 300 and 600 K for bulk GaN.

is predicted for temperatures as high as 600 K, while the room temperature peak is nearly 2.6×10^7 cm/s, which translates into a 30-percent increase over that for GaAs. These results also indicate that high-field drift velocities for the wurzite phase are larger than those reported for zinc blende GaN. Although experimental reports of the low-field

mobility demonstrate higher values for zinc blende due to a smaller Γ_L -valley effective mass, the wurtzite phase would have an advantage for high field applications. This is because the satellite valley for the wurtzite phase is higher, at around 1.95 eV versus the 1.45 eV inter-valley energy separation for zinc blende. These conclusions are similar to those reached previously by Kolník et al.¹⁰⁰ Finally, the Monte Carlo results for the lowest Σ -valley occupancy as a function of time are shown in Fig. 7 for various electric fields. Fractional occupancies of 90 percent and higher are predicted for applied electric

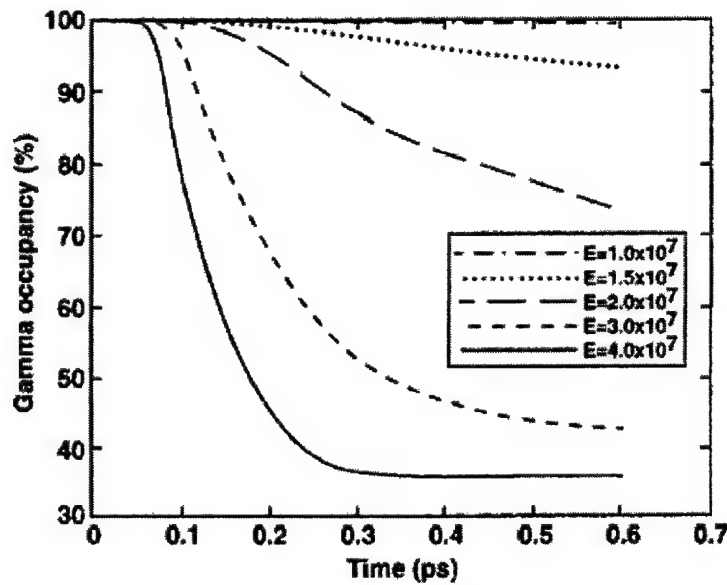


Fig. 7. Monte Carlo predictions of the time-dependent Σ -valley occupancies at different fields.

fields below 150 kV/cm. There is a relatively sharp transition into the satellite valleys for fields around 180 kV/cm. Steady-state occupancies as low as 35 percent are predicted at our highest field, 400 kV/cm. These results are also fairly close to those obtained by Kolník et al.,¹⁰⁰ on the basis of a more sophisticated Monte Carlo scheme that included a full bandstructure. This agreement establishes the validity of the transport parameters used in the present model and underscores its utility as a simple, computational efficient tool for analyzing transport for field below 400 kV/cm.

6.2 Monte Carlo Results for HEMTs

Simulations were carried out at 300 K for the GaN-AlGaN HFET structure. The polarization effect is known to be dominant in this material system, and so should influence both the carrier sheet density and interface electric field. Since the carrier density controls the device current and mitigates scattering through enhanced screening, it is critical to correctly predict the mobile charge density as a function of the geometry and operating conditions. The interface field is also an important transport parameter, since it shapes the electronic wavefunctions, thereby influencing the interface scattering process. Consequently, the sheet density and interface fields were calculated as a function of the gate bias. The AlGaN mole fraction and thickness were the variable parameters. The results are shown in Figs. 8 and 9 for an undoped system. From both

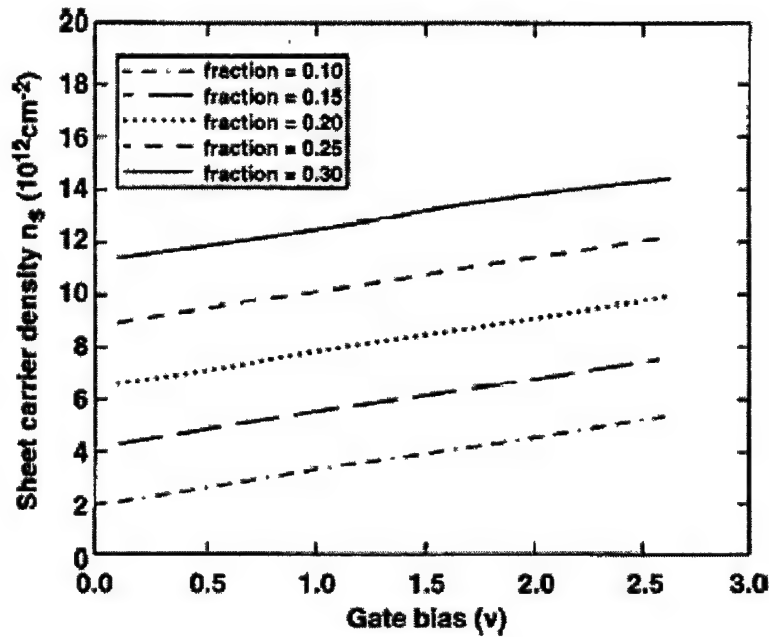


Fig. 8 Gate voltage dependence of the electron density for various AlGaN mole fractions. The thickness was 30 nm.

figures, it is evident that the 2D electron density n_s is large and almost an order of magnitude higher in comparison to values reported in the literature for the GaAs heterosystems. Our values match the recent experimental reports for the AlGaN-GaN HFET. Figure 8 for 30-nm barriers, shows that as the AlGaN mole fraction is increased,

the sheet density (and hence also the interface field) is enhanced. This is due to the increased values in both the spontaneous and piezoelectric polarization terms. Increases in the band offset with mole fraction also contribute to a higher n_s value.

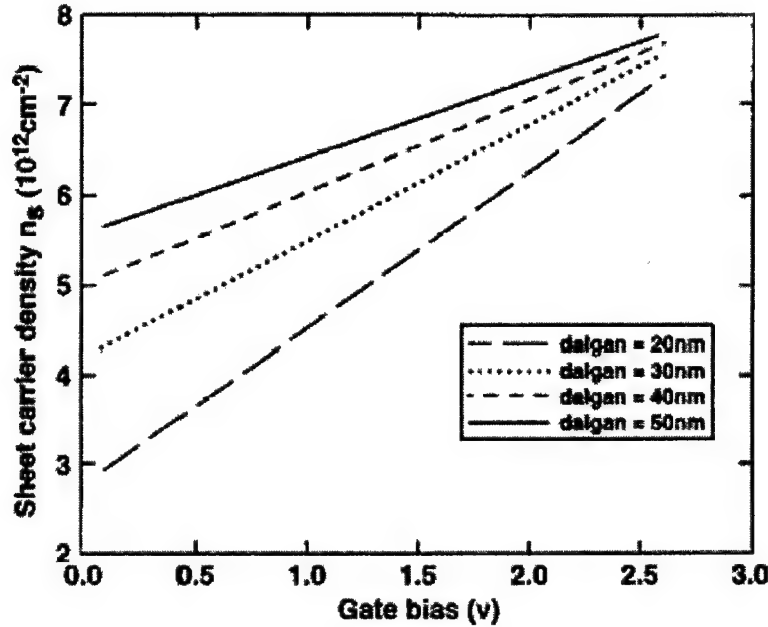


Fig. 9 Gate voltage dependence of electron density for various $\text{Al}_{0.15}\text{Ga}_{0.85}\text{N}$ layer thicknesses.

Also as expected, the density increases with bias. The four curves of Fig. 9 show the effect of variations in the AlGaIn barrier thickness on the bias-dependent sheet density. The Al mole fraction was kept fixed at 0.15. The largest barrier thickness provides the most mobile carriers in the channel. Obviously there would be a practical limit on barrier thickness increases for purposes of enhancing the channel density. With a very thick AlGaIn layer, the device would no longer be pseudomorphic and would have internal dislocations and defects.

Next, the electron channel mobility was calculated based on the Monte Carlo model. Currently there are no measured data available on the interface roughness characteristics, to the best of our knowledge. In the absence of such data, the interface roughness correlation length L , and the rms height of interface roughness fluctuations),

were taken as adjustable parameters. It was implicitly assumed that the interface roughness process could be adequately modeled in the Born approximation with the use of weak-perturbation theory, and that localization effects were negligible. Furthermore, the presence of any spatially distributed interface polarization charge arising from the creation of AlGa_{0.15}N and GaN islands at the hetero-boundary were presumed to be adequately included by the L and γ parameters. Since the mobility has to be computed at zero (or very low) electric fields, this parameter was evaluated based on the diffusion coefficient D . Use of a drift velocity calculation at low fields for determining the mobility can lead to large statistical variations, due to the low driving field. The diffusion constant was computed from the time derivative of the second central moment as :

$$D = 0.5 \, d[\langle (x_i(t) - \langle x_i(t) \rangle)^2 \rangle] / dt = dP(t) / dt \quad . \quad (38)$$

Strictly, the above applies to nondegenerate situations. For a more precise calculation of D with degeneracy, a modified Monte Carlo technique as suggested by Thobel et al.¹⁰¹ needs to be used. However, this aspect was ignored here, and instead equation (38) used for calculations of D . An approach similar to the present one was taken by Yamada et al.¹⁰² in the recent past. The low-field mobility μ is related to D via the Einstein relation¹⁰³ as $D = (n/q) [dn/dE_F]^{-1}$ where q is the electronic charge, n the carrier density, and E_F the Fermi energy. For a two-subband electron system considered here, the density n is related to the Fermi level as :

$$n = [m^* k_B T / (B \Sigma^2)] \ln[(1 + \exp\{(E_F - E_1)/(k_B T)\}) \cdot (1 + \exp\{(E_F - E_2)/(k_B T)\})] \quad , \quad (39)$$

where m^* is the effective electron mass, while E_1 and E_2 are the subband energies. With the use of the above equations, the mobility can be determined from a knowledge of the diffusion constant D . Figure 10 shows the time-dependent variation of the $P(t)$ term for various values of L and γ with applied gate bias values of 0.0 and 3.0 V. A 30-nm Al_{0.15}Ga_{0.85}N layer was used. Values of 1.5 nm and 2 nm for L , with $\gamma = 1$ and 0.75 nm, have been shown. These parameters were adjusted until a good match of the electron

mobility with available experimental data was obtained. The best mobility fit was obtained for $L = 1.5$ nm and $\Delta = 0.65$ nm. The mobility results at 300 K as a function of

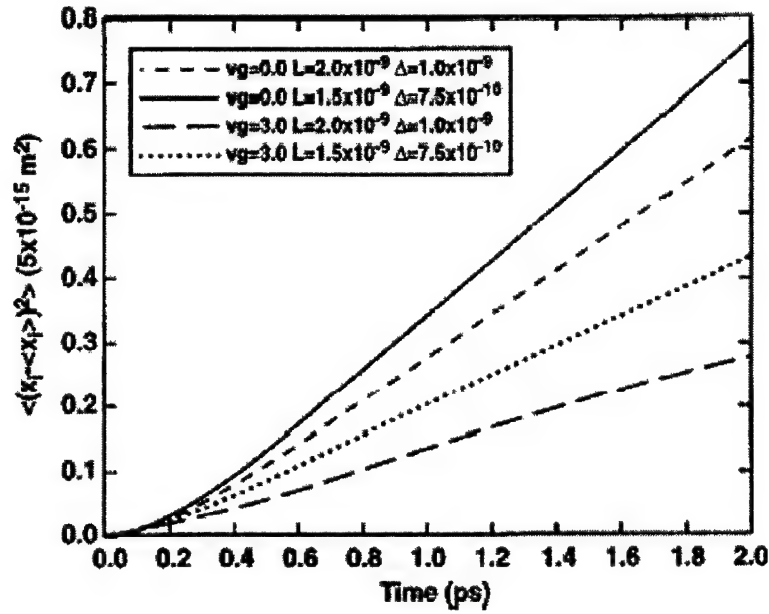


Fig. 10. Time dependence of the second central moment obtained from Monte Carlo calculations.

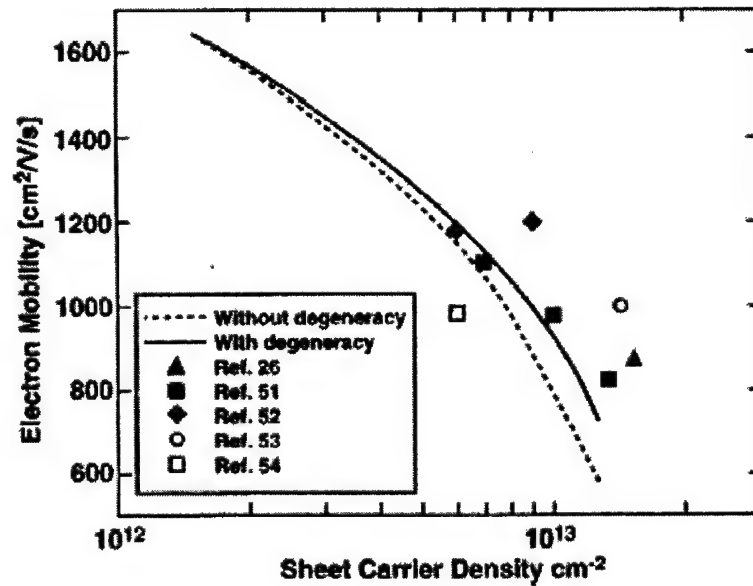


Fig. 11. Monte Carlo results of the gate-bias-dependent GaN HFET electron mobility with and without degeneracy.

gate bias are shown in Fig. 11, along with experimental data taken from the literature.¹⁰⁴⁻¹⁰⁷ The measured values do have a significant spread.

The role of degeneracy is clearly brought out in Fig. 11. Without degeneracy, the mobility is predicted to be much lower, since the possibility of final state occupancy is then discounted. The predicted values agree with the available experimental data, but only when the Pauli exclusion is taken into account. It may be mentioned that the experiments measured Hall mobility, while here the low-field drift mobility has been obtained. The two differ by the Hall factor. The Hall factor can be quite complicated, since it depends on the details of the prevalent scattering mechanisms, their relative strengths, and the bandstructure that the mobile carriers. Typically, the Hall factor has a value higher than unity. In some cases, however, such as holes in strained Si or $\text{Si}_{1-x}\text{Ge}_x$ alloys, this factor can be below unity.¹⁰⁸ This is due to the strong nonparabolicity and band warping effects. For electron in GaN, however, such a peculiar situation does not arise. Hence, the Hall factor is, in general, larger than 1. Consequently, the drift mobility is expected to be lower than the Hall mobility. This aspect was indirectly taken into account here, and the fitting parameters were chosen to yield drift mobility predictions that were somewhat lower than the experimental values.

Next, the electron drift velocity was calculated for the interface roughness parameters obtained from the fitting procedure above. The transient velocities at different values of longitudinal electric field along the channel, with the applied gate bias V_g as a parameter, are shown in Fig. 12 for 300 K. As expected, the highest velocity occurs at the lowest (0 V) gate bias, due to reduced interface roughness scattering. At electric fields of 20 and 50 kV/cm, the steady-state velocities for $V_g = 0$ are predicted to be about 1.5×10^7 and 2.1×10^7 cm/s, respectively. At the 3 V gate bias, the corresponding values for the 20 and 50 kV/cm fields are 1.15×10^7 and 1.8×10^7 cm/s. The steady-state results gleaned from the transient Monte Carlo simulations are shown in Fig. 13 for four values of the gate bias. In addition, steady-state velocity-field curves for the 2DEG at 600 K are also shown. The velocity decreases with the gate bias for every

longitudinal field value, but the scaling is not linear. This is expected, since changes in V_g primarily affect interface scattering, while the other processes are only mildly changed due to variations in the wavefunction overall and screening. In any case, it becomes clear

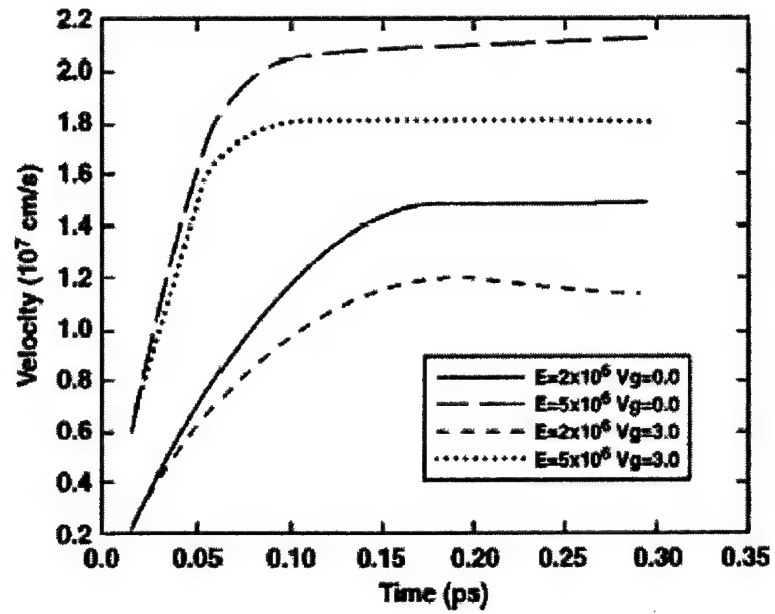


Fig. 12. Transient 2D electron drift velocities as a function of the gate bias and longitudinal electric field at 300 K.

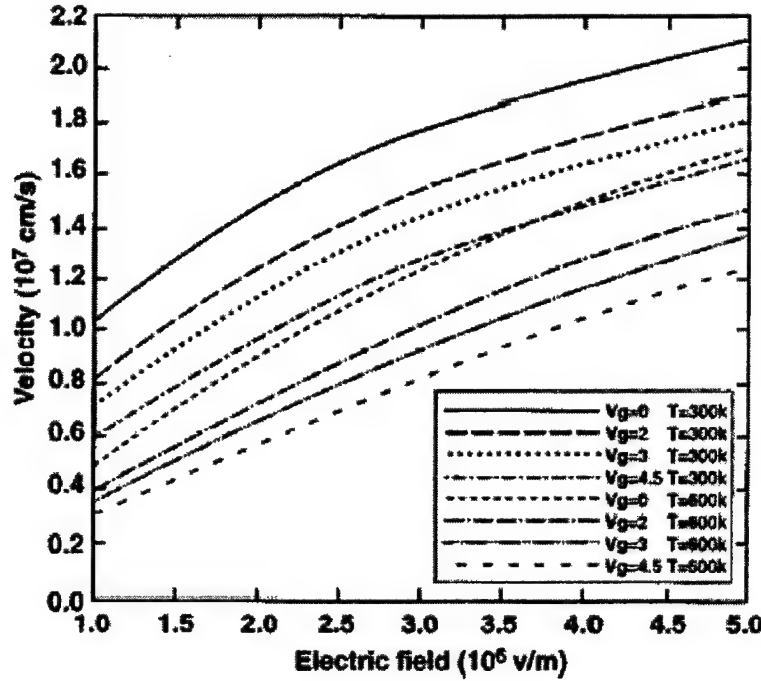


Fig. 13. Steady-state velocity-field characteristics for 2D electrons for various gate voltages. Temperatures of 300 and 600 K were used.

that the nonlinear dependence on gate voltage is likely to play a role in large signal amplification and cause mixing of multifrequency signals. The values for 600 K are lower than at 300 K, but the nonlinearity with V_g appears to be somewhat mitigated. This is to be expected, since the phonon processes become more dominant at the higher temperatures and reduce the relative role of interface roughness scattering (IRS). Since the IRS rate is strongly energy dependent and decreases sharply with increasing energy, the gate voltage effects should be most prominent under conditions of low carrier energies, such as with low longitudinal electric fields. This is borne out in Fig. 13. At the lowest electric field of 10^6 Vm^{-1} , the drift velocities V_{300} and V_{600} corresponding to temperatures of 300 and 600K, respectively, are predicted to be 1.044×10^5 and $0.4883 \times 10^5 \text{ ms}^{-1}$ for $V_g = 0$. However, at $V_g = 4.5$ Volts, the velocities V_{300} and V_{600} are computed to be 0.59×10^5 and $0.3018 \times 10^5 \text{ ms}^{-1}$, respectively. The ratio $(V_{600}/V_{300})|_{V_g=0}$ then turns out to be less than $(V_{600}/V_{300})|_{V_g=4.5}$. This inequality $(V_{600}/V_{300})|_{V_g=0} < (V_{600}/V_{300})|_{V_g=4.5}$ is the direct consequence of a disproportionately large reduction of the low-field 300 K velocity in going from the $V_g = 0$ operating condition to $V_g = 4.5$ Volts.

6.3 Monte Carlo Based Distortion Analysis

The polarization effect is known to be dominant in the GaN-Al_xGa_{1-x}N material system, and influences the carrier sheet density n_s , screening and degeneracy, the interface electric field, and the interface roughness scattering. The calculated carrier density as a function of the gate bias for an undoped system with 30 nm Al_xGa_{1-x}N barriers, has been shown in Fig. 8. It shows a negative gate threshold for each curve, making n_s a strongly nonlinear, monotonically increasing function of V_G . For analytical calculations, polynomial curve fits to the n_s - V_G relationships can easily be obtained for each mole fraction. Obviously if the HEMT were operated in the large-signal mode with amplitudes less than the gate threshold, then the nonlinearity (and hence, IMD) would be less severe. Figure 8 also indicates that increasing the mole-fraction should improve the IMD characteristics, and permit higher signal voltages and input power due to an increased gate threshold. Obviously there is a practical limit on barrier thickness increases, since for very large mole fractions, the device would no longer be pseudomorphic, and could have internal dislocations and defects.

The second source of nonlinearity arises from a V_G dependence of the 2DEG drift velocity. This aspect was probed by carrying out Monte Carlo simulations for a fixed drain field for various values of dc gate voltages. Results showing variations in the electron drift velocity v_{dr} with gate voltage are shown in Fig. 14 with the mole fraction as a parameter. The temperature was set to 300 K and a longitudinal channel field of 10 kV/cm was used. The relatively low field was chosen to avoid complications arising

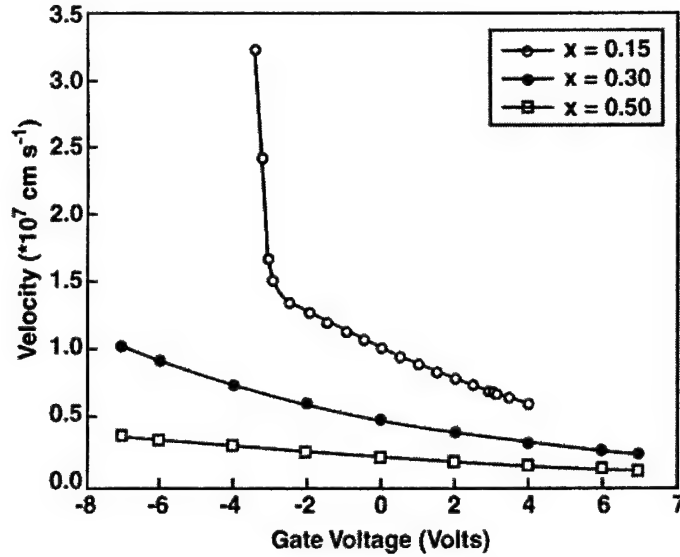


Fig. 14. Monte Carlo results of the electron drift velocity at 300 K as a function of the HEMT gate voltage with the $\text{Al}_x\text{Ga}_{1-x}\text{N}$ mole fraction as a parameter.

from real space transfer and trapping within the AlGaInN layer. Such secondary effects have been reported recently at high drain currents.⁹⁸ A general monotonic decrease of the carrier velocity with gate voltage is apparent, and arises from increases in interface roughness scattering (IRS). Since the decreasing v_{dr} behavior is opposite to the n_s trend, these two factors mitigate the overall nonlinearity in the current. Based on the above argument, one can expect the nonlinear response trend to change at higher temperatures. This is because at higher temperatures, phonon scattering would increase, reducing the role of IRS. Consequently, the decrease in v_{dr} with gate voltage would become less significant, and the n_s - V_G term would dominate. The V_G dependence of the current density was obtained by combining the results of Figs. 8 and 14 for various values of the mole fraction. The results are shown in Fig. 15. The $x=0.15$ curve is dominated by the electron density term. It has a strongly non-linear current density with values starting near zero close to the -3.5 Volt threshold. This is followed by a significant increase. The $x=0.5$ curve allows for a much larger gate voltage swing, and is dominated by the velocity term since carrier density does not change much over this range of V_G . A monotonically decreasing trend results. Finally, the $x=0.3$ curve exhibits an initial increase due to the n_s term, followed by a decrease arising from the drift velocity factor. In general, the results exhibit the following features. (a) All curves exhibit non-linearity.

(b) The characteristics change with the mole fraction and the gate voltage swing. For example, the $x=0.3$ curve reveals that a large-signal gate amplitude limited to ± 2 Volts would produce a nearly constant current response. For these conditions then, output power at the fundamental frequency can be expected to be relatively low. (c) The results of Fig. 15 suggest the possibility of judiciously selecting conditions for minimal non-linear distortions.

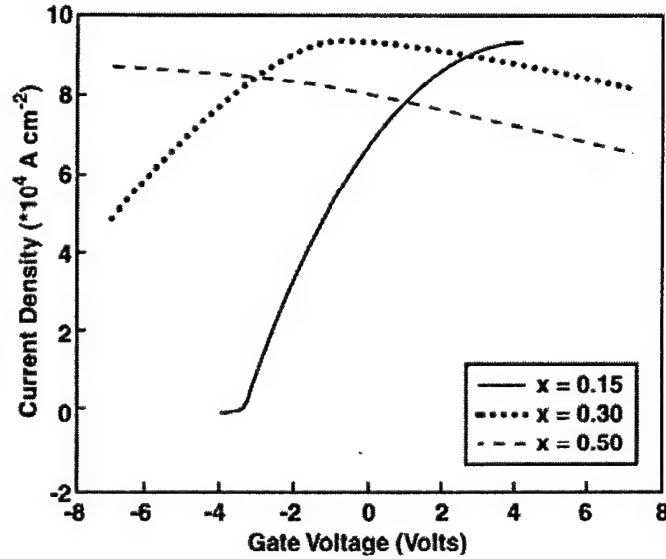


Fig. 15. Current density dependence on the gate voltage at 300 K for various $\text{Al}_x\text{Ga}_{1-x}\text{N}$ mole fractions.

The input-output power characteristics are shown in Fig. 16. Polynomial fits to the voltage dependent current densities of Fig. 15 were used to generate the power

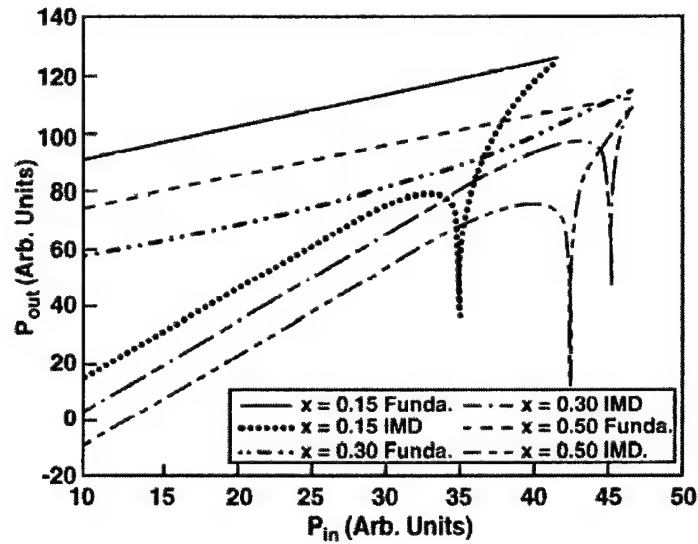


Fig. 16. Calculated output-input power characteristics for the fundamental and third-order inter-modulation frequencies. Mole fractions of 0.15, 0.30 and 0.50 were used for the barrier layer.

characteristics for $x=0.15$, 0.30 and 0.50. Values of P_{in} on the x-axis were calculated as: $P_{in} = 10 \log_{10}(10^3 * A^2)$ with A being the gate voltage amplitude. Similarly, values of P_o were obtained as: $P_o = 10 \log_{10}(10^3 * J^2)$ from the computed drain current density J . The following features of interest can be discerned from Fig. 16. (i) The third-order intermodulation curves exhibit a local minima for all three mole fractions. Such behavior has been reported for GaAs transistors⁹⁶ and so, is consistent with experimental observations. At low input power, the curves all follow the simplified theory that predicts a constant 3 dB increment in distortion for every decibel of input power. (ii) For optimal results, it would clearly be best to operate the device at an input power level that corresponds to the IMD minima, since the differential between the fundamental and IMD outputs is then the greatest. This, in theory, would allow for superior device operation at relatively input powers larger than predicted by a conventional assessment. (iii) The lowest power output at the fundamental frequency is for the $x=0.3$ case. This outcome is expected from Fig. 15, which as discussed previously, reveals a nearly constant current response for large signal amplitudes limited to 2 Volts. By the same reasoning, the fundamental output for $x=0.15$ is the best, since the corresponding curve of Fig. 15 has the most linear characteristic of the three. (iv) Despite low output power at the

fundamental for $x=0.3$, there would seem to be two inherent advantages. First, the characteristics are predicted to have gain expansion at higher voltages. Such gain expansion has been reported in the literature¹⁰⁹. Second, the operating power corresponding to the IMD minima is the largest for $x=0.3$.

The large-signal response at an elevated temperature of 600 Kelvin was analyzed next for a relative comparison with room temperature results. Simulation predictions obtained for the current density as a function of V_G are shown in Fig. 17 for $x=0.15$. As expected, the 300 K curve (the same as shown in Fig. 15) is generally higher due to increased

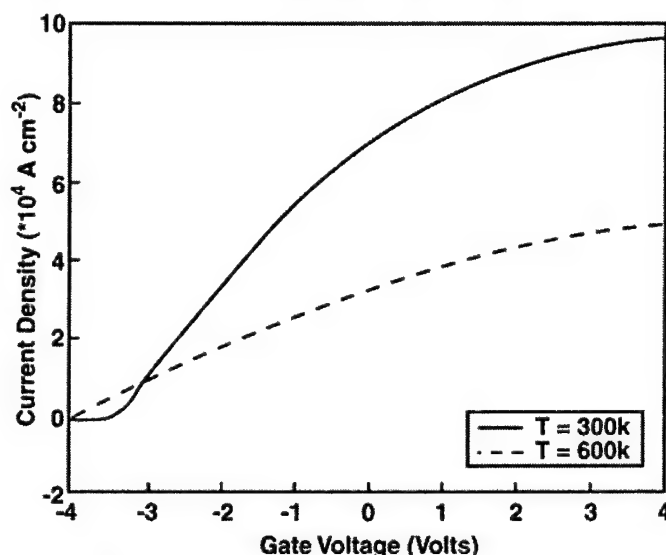


Fig. 17. Comparison of the calculated V_G dependent current density at 300 and 600 Kelvin for an Aluminum mole fraction of 0.15.

carrier drift velocity resulting from lower phonon scattering, except near the V_G threshold. Carrier densities at the two temperatures are nearly the same, except for a slightly more negative gate threshold for the 600 K case. Hence, the curves are generally controlled by the carrier drift term, but show a somewhat larger current at 600 K close to the gate threshold value. Furthermore, since phonon scattering is strongly temperature dependent, while interface roughness scattering is not, the relative role of IRS is reduced at 600 K. Hence, for the 600 K case, the velocity variation (and thus the current density) tends to flatten out, showing a weak V_G dependence at the larger gate voltages. Overall, the 600 K characteristic is smoother, and is perhaps a closer approximation to a linear curve as compared to the 300 K result. Thus crudely, one might expect lower distortion

for higher temperature operation. The input-output power characteristics obtained through polynomial curve fits to the data of Fig. 17 are shown in Fig. 18. Looking only at the fundamental frequency, the output power at 300K exceeds that at 600K. This in itself seemingly favors room temperature operation. This result is the direct consequence of a greater drift velocity and hence, device current, at 300K due to lower total scattering. However, the IP3 curve for 600 K is substantially smaller than the corresponding 300K characteristic and exhibits a much larger differential. Thus, for better device performance in terms of an IP3 differential alone, the 600 Kelvin operation seems to be the favored alternative. Furthermore, the fundamental and IP3 curves at 300 K are seen to intersect over the input range considered, while those for 600K do not. These results are thus indicative of potential benefits for device operation at elevated temperatures.

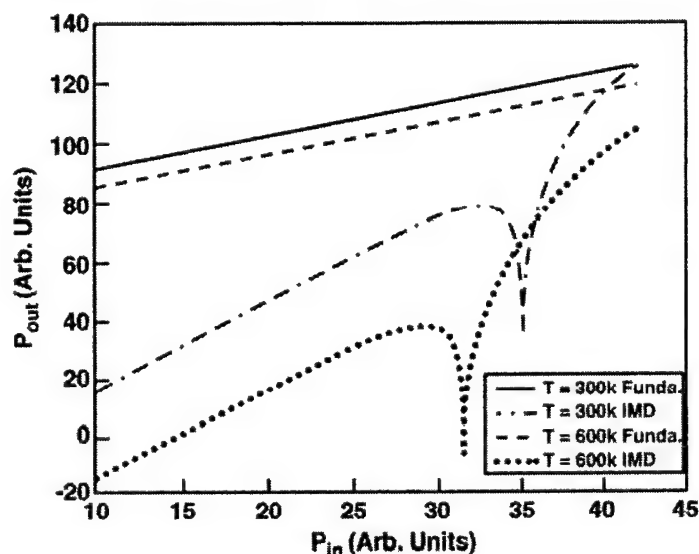


Fig. 18. Comparison of the calculated output-input power characteristics for the fundamental and third-order intermodulation frequencies at 300K and 600 K. A mole fraction of 0.15 was used.

Finally, direct full-Monte Carlo calculations for the HEMT were performed to gauge the response to two-tone, large-signal inputs. Instead of using polynomial fits to the steady-state velocity-field data as generated by a Monte Carlo calculation, a full dynamic MC simulation of the current response to a two-tone, time varying signal was performed. The MC-based approach was undertaken for the following reasons. (i) It provides a much better dynamical treatment of the carrier transport. (ii) The results serve as a

validity check to the analytical fits. (iii) All memory effects, which were absent from the polynomial expressions, could be included. Also, in effect, this naturally allowed a voltage dependence to the various coefficients K_i . (iv) The inclusion of distributed internal effects. In the analytical approach it is assumed that the current changes instantaneously in response to the applied signal uniformly. The MC, however, takes account of the spatial distributions and temporal delays. The results for the fundamental and IP3 are shown in Fig. 19 at 300 K for $x=0.15$. Running the MC simulator for a discrete set of V_G large-signal amplitudes generated the required data points. The time-dependent current density response was recorded for each input two-tone signal. Due to

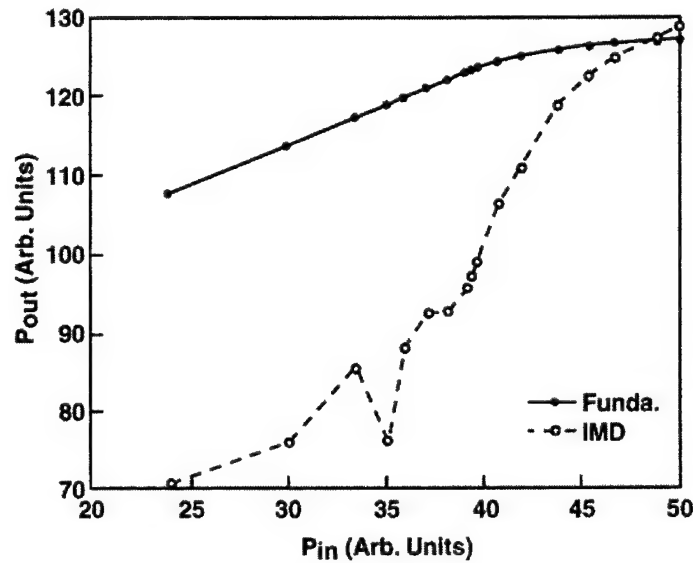


Fig. 19. Direct Monte Carlo results of the output-input power characteristics at 300K for a mole fraction of 0.15.

the computationally intensive nature of the simulations, only a few discrete V_G amplitudes were chosen. The use of relatively few V_G points, coupled with the statistical nature of the MC simulation, yielded curves that were less smooth compared to those of Fig. 16 that resulted from the analytical fits. Similarities between the curves of Fig. 16 and the 300K analytical results of Fig. 18 are apparent. In both cases, the IMD minima occurs at a value of about 35, though the analytical curve of Fig. 16 is much smoother. Minor differences include a more pronounced saturation (especially at the fundamental) and a higher cross-over point from the Monte Carlo calculations. The disparity is

indicative of the internal memory and distributed effects that only the MC calculations can fully account.

6.4 Analytical Assessment for IP3 and Distortion

Equation (37) reveals that the requirements for reduced inter-modulation distortion, increased gain, and maximization of the IP3 point are increases in Z , C_0 , C_1 and $T_1(x)$, with corresponding reductions in $T_2(x)$. The latter can be attained either by designing $C_2 \rightarrow 0$ and $C_3 \rightarrow 0$, or more realistically, by *ensuring that C_2 and C_3 have opposite sign*. From a physical device standpoint, possibilities for achieving a large IP3 dynamic range then amount to the following: (i) Reducing the channel length L so that $[K_1/\{L+V_D K_2\}] \rightarrow K_1/(V_D K_2) \rightarrow v_{sat}/V_D$. This would almost be a fixed value (for a given temperature) with only a weak dependence on V_D . (ii) Attempting to increase the barrier height for reductions in real space transfer (RST), thereby mitigating the role of gate voltage on the transport characteristics. This can be achieved either by increasing the mole fraction or inserting a very thin AlN interfacial layer as recently reported by Shen et al.¹¹⁰ The suppression of RST would effectively make v_{sat} nearly independent of V_G , as there would only be one conduction channel with the GaN region. (iii) High temperature operation since the role of phonon scattering then increases, while the relative contribution of interface roughness scattering (and hence, V_G) is reduced. (iv) Choosing a mole fraction x so that the channel carrier density does not reduce to zero even at the least negative V_G point. On the basis of eqn. (26), this implies: $B_{10}(x) > [\{_{,0}(x)/d\}|V_G| + 0.5 B_2(x) V_D]$. Mathematically, this translates into a lower-bound for x depending on the maximum operating bias V_D and gate voltage swing “A” assigned for a given application. Using the mathematical expressions given previously, yields the following inequality for improving the dynamic range:

$$0.0483x \{ [(5x + 103)/(-32x + 405)] (0.73x + 0.73) + (0.11x + 0.49) \} + 0.052x > [8.85 \times 10^{-12} (9.5 - 0.5x)/d] \{ 0.84 + 0.103x - 0.7x^2 + |V_G| + 0.5 V_{DS} \} , \quad (40)$$

Using typical upperbounds of 10 Volts for V_{DS} and 2.5 for V_G , the mole fraction needs to be greater than 0.22 for 25 nm AlGaIn thickness and above 0.49 for a 10 nm AlGaIn

layer. This simple calculation helps bring out an inherent advantage of the GaN HEMT for microwave applications. As is evident, the existence of a polarization induced interface charge density $s_s(x)$, enhances $B_{10}(x)$, thereby making it possible to avoid a sharp fall-off in the channel charge for more negative gate voltages even under large drain bias conditions. There is thus, a significant advantage over traditional GaAs-based MESFETs or pseudomorphic HEMTs.

The coefficients C_i were extracted from Monte Carlo simulations of the electron drift velocity characteristics. For purposes of evaluating the effects of real space transfer (RST) on devices behavior, Monte Carlo simulations for again carried out at 300 K. The corresponding steady-state velocity-field curves so obtained are shown in Fig. 20. For comparison, results without RST are also included. The RST simulations were carried out by allowing for electron transfers into and out of the AlGaIn barrier layer. The AlGaIn layer was treated as a bulk semiconductor, and quantization effects ignored for electronic transport in this region. The velocity-field (v - E) curves of Fig. 20, have minimal

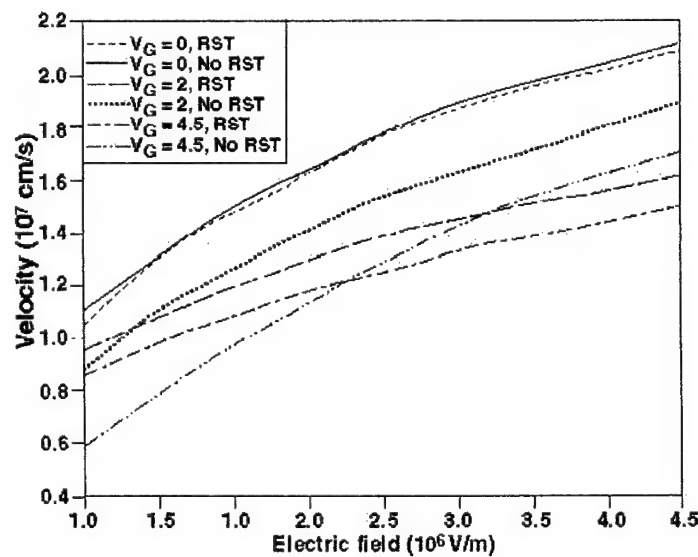


Fig. 20. Monte Carlo calculations of velocity-field curves with inclusion of real space transfer at 300 K.

difference at $V_G = 0$. With increasing gate voltage, the v - E curves are predicted to exhibit gradual reductions in slope for the RST situation. This is consistent with the notion of reduced “overall mobility” associated with parallel conduction in both bulk AlGaIn and the GaN channel. For high V_G , however, the RST velocities are somewhat larger at the lowest electric fields. This is indicative of lower overall scattering, and is associated with the two following effects. First, interface roughness scattering is absent for the electronic population undergoing bulk AlGaIn transport. Second, at low electric fields the carrier energies are lower leading to the reduced probability of phonon emission processes. This is especially relevant for this material system given the relatively high optical phonon energy.

The Monte Carlo velocity-field curves for a barrier layer mole fraction of 0.15 were used to determine the fitting parameters $K_1\{V_G\}$ and $K_2\{V_G\}$ of eqn. (31). Results of the curve fitting at 300 K and 600 K with and without the inclusion of real space transfer (RST) are given in Tables II(a)-II(c). Based on the data presented in Tables II(a)-(c), it becomes evident that the variation in the parameterized ratio $R (=K_1/K_2)$ is the least for the 600 K case, and the most for at 300 K with inclusion of real space transfer. For example from Table II(c), $R\{600K, \text{No RST}\}$ has a very modest variation, only changing from 3.6×10^5 at $V_G = 0$ to 3.67×10^5 for $V_G = 4.5$ V. The deviation in $R\{300K, \text{RST}\}$ for the corresponding gate voltages is from 2.766×10^5 to 1.946×10^5 , while $R\{300K, \text{No RST}\}$ ranges from 2.6478×10^5 to 3.475×10^5 . The nearly constant value of R at 600K obtained here bodes well for reducing gate-voltage related non-linear distortions and inter-modulation effects. So at least for small channel devices, microwave performance can be expected to improve at higher operating temperatures. This is in keeping with the previously stated expectation of a relative decrease in the role of interface-roughness scattering. The results at 300 K, reveal two shortcomings associated with the real space transfer process. First, the variation in R with V_G is higher in the presence of RST. This is seen more clearly from the following parameterized fit for R at 300 K from the data:

$$R\{T=300, \text{No RST}\} = 2.64 \times 10^5 [1 - 0.142 V_G + 0.0867 V_G^2 - 0.00875 V_G^3] , \quad (41a)$$

$$\text{and } R\{T=300, \text{RST}\} = 2.77 \times 10^5 [1 - 0.3646 V_G + 0.1325 V_G^2 - 0.01469 V_G^3] . \quad (41b)$$

Table II(a)**Temperature = 300 K , No real space transfer ; $x = 0.15$**

V_G (volts)	0.0	2.0	3.0	4.5
$K_1\{V_G\}$	1.88×10^{-1}	1.23×10^{-1}	0.944×10^{-1}	0.695×10^{-1}
$K_2\{V_G\}$	7.1×10^{-7}	4.7×10^{-7}	3.2×10^{-7}	2.0×10^{-7}

Table II(b)**Temperature = 300 K , With real space transfer ; $x = 0.15$**

V_G (volts)	0.0	2.0	3.0	4.5
$K_1\{V_G\}$	1.66×10^{-1}	1.77×10^{-1}	1.44×10^{-1}	1.45×10^{-1}
$K_2\{V_G\}$	6.0×10^{-7}	9.4×10^{-7}	7.4×10^{-7}	7.45×10^{-7}

Table II(c)**Temperature = 600 K , No real space transfer ; $x = 0.15$**

V_G (volts)	0.0	2.0	3.0	4.5
$K_1\{V_G\}$	0.648×10^{-1}	0.484×10^{-1}	0.412×10^{-1}	0.367×10^{-1}
$K_2\{V_G\}$	1.8×10^{-7}	1.3×10^{-7}	0.9×10^{-7}	1.0×10^{-7}

The higher order non-linear coefficients are obviously larger with RST. Second, in the presence of RST, the value of R decreases with increasing V_G . Such a trend can be expected to adversely affect the gain and current throughput of the device for microwave signals with a large voltage swing. Thus, it seems apparent that for enhancing the microwave performance of GaN HEMTs, RST should be minimized, and hence, concepts such as the inclusion of thin AlN barrier layers seem very beneficial.

6.5 Transport Calculations For GaN Gunn Structures

Having validated the Monte Carlo model, simulations were then carried out at 300 K for the GaN based Gunn oscillator based on a n^+-n-n^+ notch structure for lengths of the n -region around 1.0 μm . The much smaller length (as compared to the 3.0 μm device simulations previously reported⁴³) serves two purposes: (a) Enhanced operating frequency due to lower transit times, and (b) ensures a higher sinusoidal component at the fundamental mode. Longer devices that operate in dipole domain mode tend to have a flatter response, with a higher non-sinusoidal component since variations in terminal current only take place at the start of every domain formation cycle. The n -doping range of $5 \times 10^{22} \text{ m}^{-3} - 2 \times 10^{23} \text{ m}^{-3}$ chosen here, leads to a “ nL ” product above the $5 \times 10^{16} \text{ m}^{-2}$ threshold⁴⁷ for GaN Gunn oscillations. For a more realistic simulation of the microwave oscillator, the GaN device was embedded in a parallel resonant circuit as shown in Fig. 21a. This allows for the inclusion of circuit effects, permits performance evaluation at the fundamental frequency and other harmonics, and the assessment of circuit parameter variations. Time-varying voltage boundary conditions were applied to the GaN structure, and the device currents computed based on the Monte Carlo particle flows. The total current obtained by solving the related Kirchhoff equations. The displacement current can be accounted by using the cold capacitance procedure¹¹¹. In our simulations, the device structure was taken to have a cross-sectional area of 10^{-9} m^2 . The doping profile for the conventional notch-type device is shown in Fig. 21b. The two heavily doped end regions with densities of $2 \times 10^{24} \text{ m}^{-3}$ serve as the n^+ contacts. The doping level “ n ” of the transit region was taken to vary within the $5 \times 10^{22} \text{ m}^{-3} - 2 \times 10^{23} \text{ m}^{-3}$ range. Thus, the doping level of the drift region was chosen to be much larger than typically used for GaAs or InP Gunn devices^{112,113}. Since the mobility of GaN is lower in comparison to

both GaAs and InP, the time required to build up a stable domain is higher for the same background doping. The higher doping chosen here, helps offset the lower mobility value. The notch at the cathode end is required to create the local nonuniformity that helps launch the accumulation or dipole-domain mode instabilities. The equilibrium density of the notch was set at 20 percent of the transit region. The dead-zone lies in this region. Fig. 21c shows the schematic of a repetitive Gunn diode structure with three transit regions. Such structures with multiple zones were also used in the present simulations. For the electrical circuit, a 20 Ohm resistor, an external capacitance of 0.05 pF and a 0.12 nH inductor were assumed.

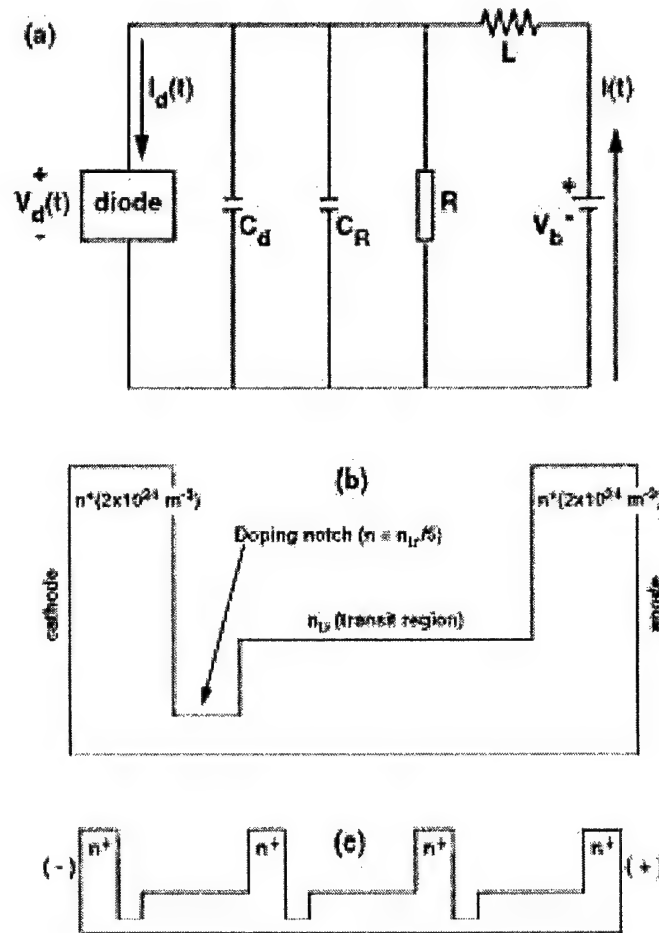


Fig. 21. Schematic pertaining to the device simulations. (a) Lumped electrical circuit, (b) Doping profile of the conventional GaN notch diode, and (c) Schematic of a three transit region multiple GaN Gunn diode.

The circuit of Fig. 21 was incorporated and the initial electron distribution taken to mimic the doping density distribution. The Gunn structure was taken to connect with the tank circuit at $t=0^+$. Monte Carlo results at 300K for the single transit Gunn diode showing the time dependent behavior of the total current and the device voltage are shown in Fig. 22. The device length was taken to be 1.0 :m, and applied bias was 50 Volts. The initial transient is simply associated with the commencement of the applied dc bias at time $t = 0$. A steady oscillatory state is reached in about 60 picoseconds, with the operating frequency predicted to be 135 GHz. Results for the simulated frequency dependencies of the generated power and device efficiency were then obtained by running such time dependent simulations for various device voltages, device lengths and operating temperatures. The results are given in Figs. 23 and 24, for two operating

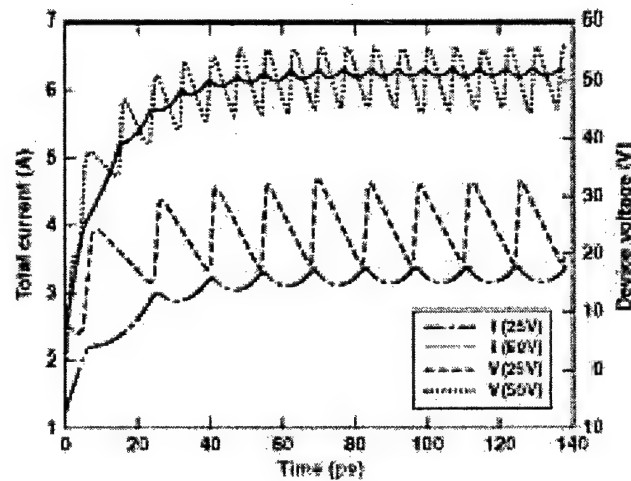


Fig. 22. Simulation results showing the temporal development of the device voltage and total circuit current for a 1.0 micron device at 300K. A 50 Volt bias was used.

temperatures of 300 K and 450 K. At very low biasing levels, the electric field within the GaN device is close to the threshold for NDR, and hence, the power output is low. With increasing bias the output power increases, as does the operating frequency due to the larger average electron velocity. A central maxima thus results, and the general shape is in keeping with previous reports. At very high biasing the transferred electron effect is lost with nearly all carriers residing primarily in the satellite valleys. The curve at the higher temperature of 450 K shifts to lower frequencies due to the reduced carrier velocity and the power output is predicted to drop. Fig. 23 shows peak powers to be

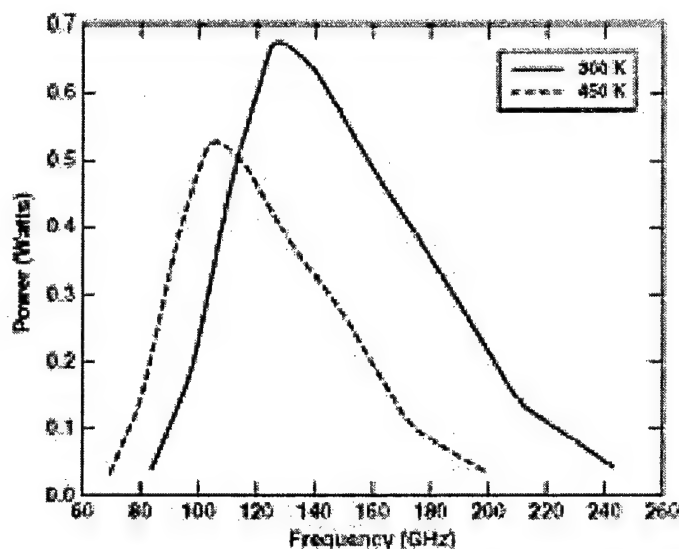


Fig. 23. Monte Carlo results of the power output versus frequency at 300K and 450 K for single domain GaN Gunn diodes.

about 0.665 W and 0.525 W at the 300 K and 450K operating temperatures. Since device self-heating effects have not been included here, these values represent an overestimation. In any case, there is considerable improvement over the reported results of about 0.150 W for InP¹¹⁴. This is not surprising, since the threshold field for GaN is roughly ten times larger than in InP. The corresponding efficiencies are shown in Fig. 24 at the 300K and 450 K temperatures. Peak efficiencies of 1.9 % and 1.47 % are predicted for the single transit region GaN Gunn diode. The room temperature value is higher than that reported for GaAs devices¹¹².

Finally, Monte Carlo simulations were performed for GaN diodes with multiple transit segments. The resulting power output as a function of the frequency is given in Fig. 25 at 300 K for one, two, and four transit regions. A simplistic expectation is for the output power to scale as N^2 (with N the number of segments) for fixed values of the operating frequency, temperature, and device impedance. This follows from a required scaling in both the voltage (to maintain the device electric fields) and device current (due to an increase in area for maintaining the impedance). However, in practice, the benefits of a multiple transit structure might not be quite as significant for a variety of reasons. In

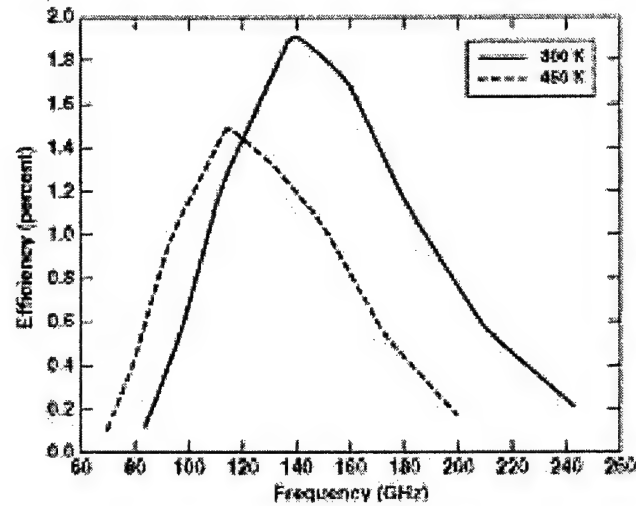


Fig. 24. Simulation results of the device efficiency versus frequency at 300K and 450 K.

a conventional single-transit region device, the injected carriers are all nearly thermalized, and have comparable energies. Hence, the device noise can be expected to be lower due to a relatively “tightly-bunched” carrier distribution, especially for short device lengths. With multiple transit zones, however, the carrier distributions at the start

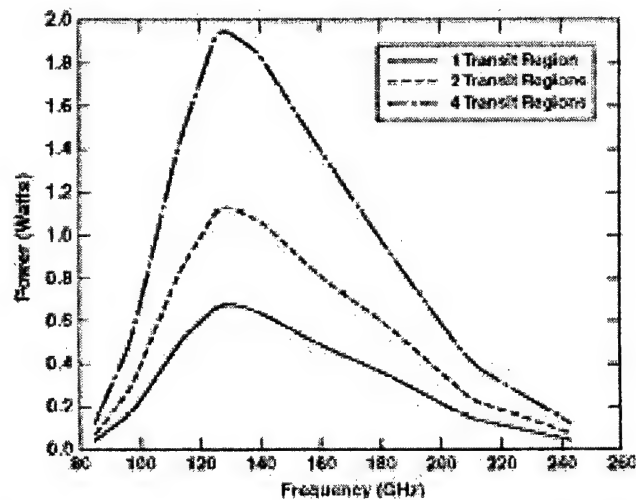


Fig. 25. Results of the power output versus frequency at 300K for multiple transit segment GaN Gunn diodes. Plots for one, two and four segments are shown.

of each successive transit segment might not be completely periodic, nor closely bunched in distribution, and could be non-thermal. Consequently, one can expect a larger variance

in the intervalley transfer distance, leading to higher noise. The actual condition at the start of successive domains depends on the thickness and doping of N^+ layer between the transit regions. Thicker and more strongly doped layers would facilitate better carrier thermalization, but would increase the overall transit time and adversely impact the operating frequency. The absence of a fully thermal distribution at the beginning of each successive transit region, also implies that the average carrier energies within the device would tend to be larger. This could lead to higher internal power losses because of strong polar-optical phonon scattering, especially within the satellite valleys due to their higher density of states. In addition, with the hot electrons spending a longer fraction of their time within the satellite valleys, the overall speed would be slower, and the swing in the current oscillation reduced. Last, but not least, the higher power losses can be expected to lead to higher internal temperatures and possible thermal gradients due to local hot spots near the successive “virtual anodes”. Both would adversely affect the transport and reduce operating frequency. Collectively then, the useful power output might not scale quite as well as N^2 .

Most of the above issues could be addressed by a three-dimensional Monte Carlo simulation procedure. However, since we have not performed self-consistent electro-thermal calculations, the heating aspects and their role in mitigating the Gunn diode response could not be addressed. The thermal analysis as well as the noise characteristics will be presented elsewhere. The Monte Carlo results of the power output versus frequency are given in Fig. 25 at 300 K for one, two, and four transit regions. The device area, however, was not increased for ease of comparison. The results show that the output power does not quite scale as N , but instead is a sub-linear function. Hence, by increasing the area, one would not expect the output power enhancement to be quite as large as N^2 . In any case, the power output is certainly better than that of the conventional, single-transit structure, and so the multiple GaN Gunn diode structure does merit serious experimental study.

6.6 Transport Effects in GaN HEMTs With Dislocation Scattering

In order to probe dislocation scattering effects, a simple HEMT structure consisting of an undoped 20 nm $Al_{0.1}Ga_{0.9}N$ barrier on GaN was assumed. Surface donor states of

density $5 \times 10^{12} \text{ cm}^{-2}$ with an activation energy of 1.4 eV were assumed. Fig. 26 shows the resulting zero-bias energy band diagram for this structure. A net 2DEG of $1.6566 \times 10^{12} \text{ cm}^{-2}$ resulted, with a spatial distribution given in Fig. 27. Due to the finite barrier height, some non-zero electron concentrations in the $\text{Al}_{0.1}\text{Ga}_{0.9}\text{N}$ layer are obvious. A relatively low mole fraction was used to reduce the lattice mismatch and hence, the strain within the layers. The associated electronic wavefunctions for the above HEMT structure for the first three subbands is shown in Fig. 28. The eigen-energies of these three subbands were found to be 7.9068 meV, 57.34 meV, and 81.238 meV, respectively. The parameters b_0 and b_1 given in eqn. (9) for the envelope wavefunctions were then obtained from the plots of Fig. 28, through a simple least-square fitting procedure. Thus, $b_0 \sim 1.1428 \times 10^9 \text{ m}^{-1}$ and $b_1 \sim 7.634 \times 10^8 \text{ m}^{-1}$.

The electron mobility in the HEMT channel for the above device consisting of an undoped 20 nm $\text{Al}_{0.1}\text{Ga}_{0.9}\text{N}$ barrier on GaN, was next obtained through Monte Carlo

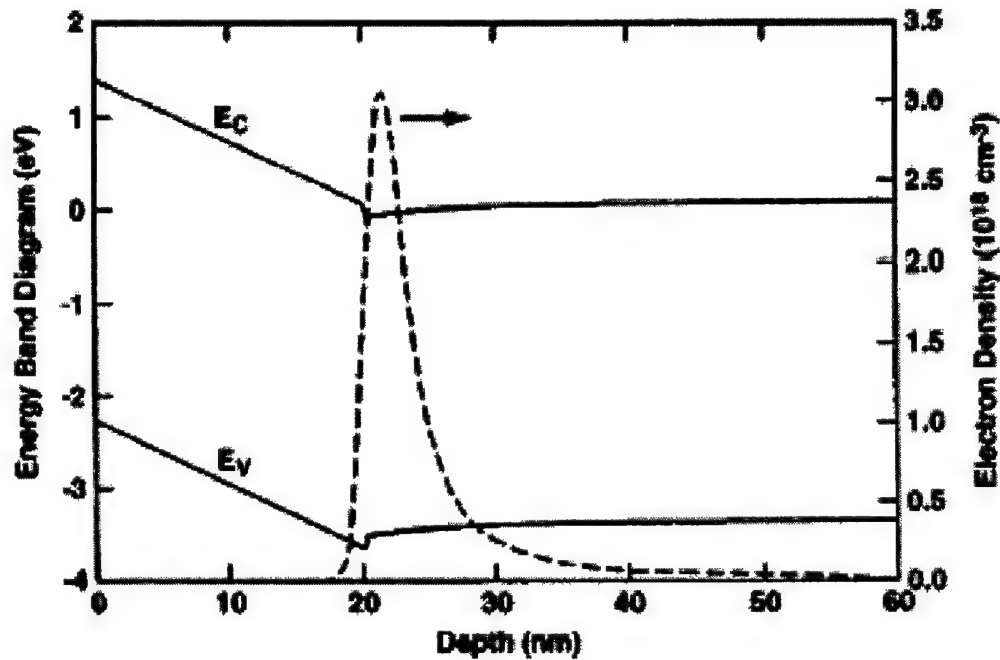


Fig. 26. Energy-band diagram of an undoped, unbiased GaN- $\text{Al}_{0.1}\text{Ga}_{0.9}\text{N}$ HEMT structure. The electron density distribution within the HEMT is also structure are shown.

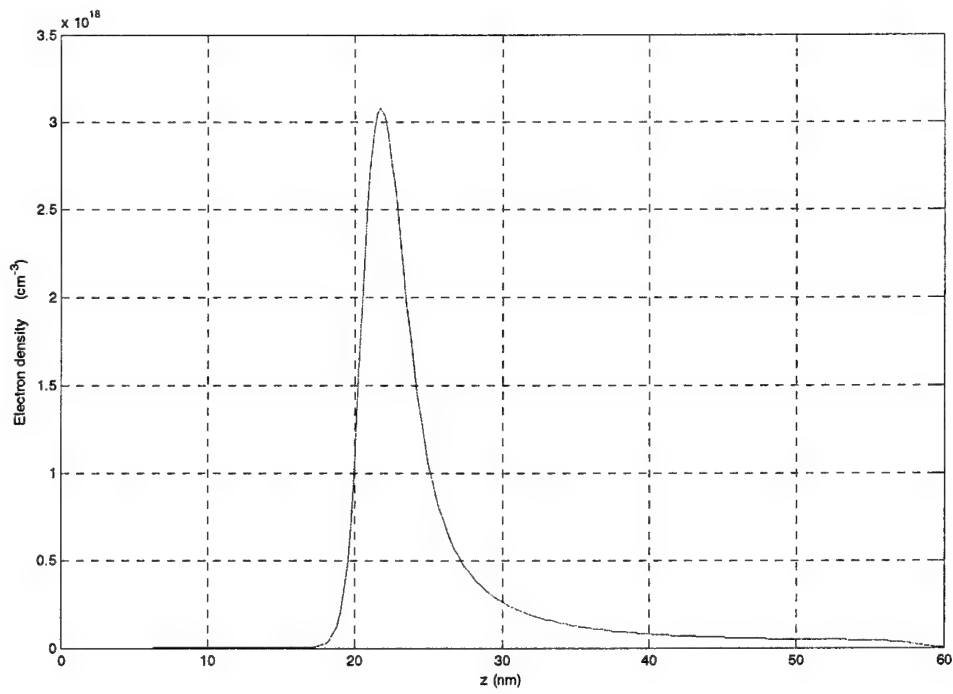


Fig. 27. Electron density distribution within the HEMT structure.

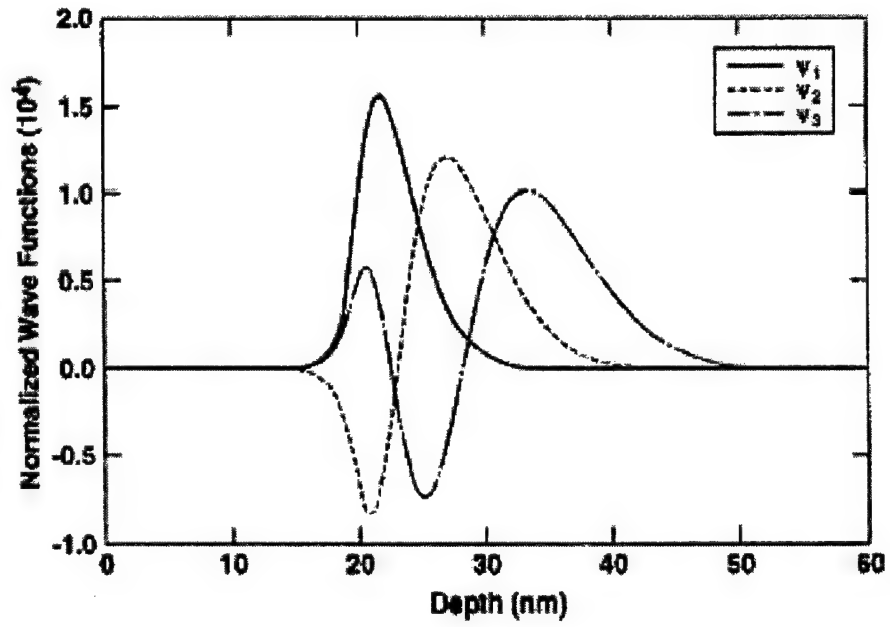


Fig. 28. Electronic wavefunctions for the first three subbands.

simulations. The results as a function of lattice temperature are shown in Fig. 29 with the dislocation density N_{dis} as a parameter. As might be expected, mobilities in the absence of dislocations are the highest. Their room temperature value is predicted to be around $1.711 \times 10^3 \text{ cm}^2/\text{Vs}$, which is fairly close agreement with the experimental data reported by the Santa Barbara group^{80, 115}. At 77 K, the highest channel mobility was obtained at about $8.440 \times 10^3 \text{ cm}^2/\text{Vs}$. This is somewhat lower than the experimental report, and is probably due to our over-estimation of interface roughness scattering (IRS). At the highest dislocation density of 10^{10} cm^{-2} , mobility reduction of 16.8 percent and 8.6 per-

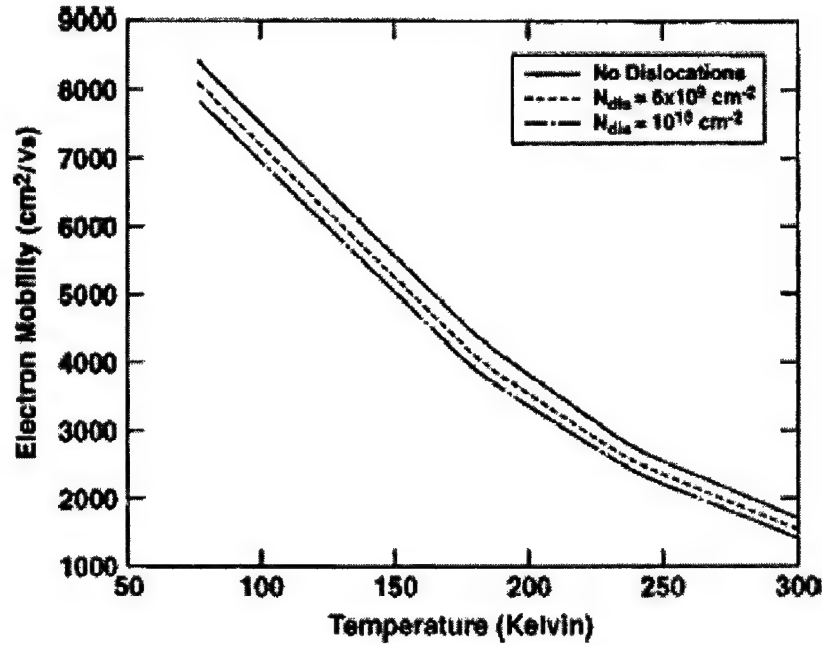


Fig. 29. Electron mobility versus temperature with dislocation density as a parameter.

cent are predicted for 77 K and 300 K, respectively. Given the sharp drop in phonon scattering at the lower temperature, the impact of dislocation scattering is relatively higher.

Finally, Monte Carlo results for the electron mobility as a function of the 2DEG density are shown in Fig. 30 for operating temperatures of 300K and 77 K. A monotonic decrease in mobility with channel density is evident at both temperatures for the density range chosen. This trend is in keeping with experimental observations^{80,115} and results from increased carrier scattering. Electric fields at the hetero-interface increase with

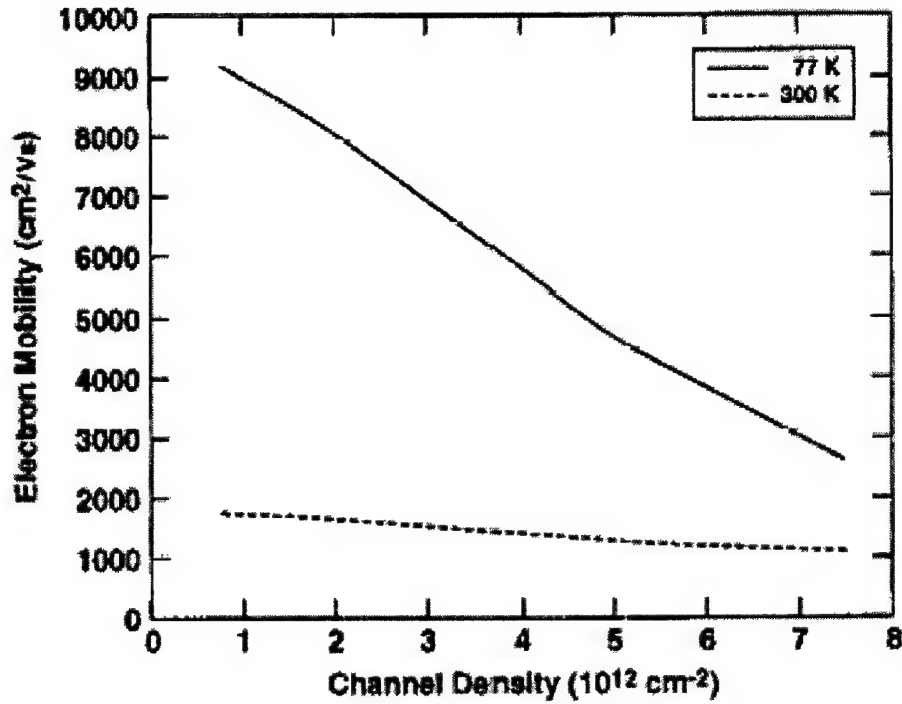


Fig. 30. Electron mobility vs 2DEG density for temperatures of 77 K and 300 K.

density, and hence, carriers are more strongly confined. This leads to enhancements in interface roughness scattering. Furthermore, the interaction with optical phonons also increases, but is not as strongly dependent on density. The mobility decrease with density is the largest at the lower 77 K temperature, since the relative impact of IRS is stronger than at 300 K. The very high density regime has not been probed here. It is conceivable that at high densities, the Fermi level (E_F) can begin to exceed the sub-band energy E_j . This could then change the phonon scattering magnitudes as $E_F - E_j \sim \Sigma T_0$ due to contributions arising from the phonon emission process.¹¹⁶ However, the behavior at 77 K and lower temperatures is not expected to be affected, and the trend predicted here should remain.

7. SUMMARIZING CONCLUSIONS

Calculations of the electronic mobility and drift velocity have been carried out for bulk GaN and AlGaIn-GaN heterojunctions based on a Monte Carlo approach. The bulk

calculations were intended to serve as a validity check of the simulation model. For the heterojunction electron mobility calculations, polarization effects, degeneracy, and interface roughness scattering were all taken into account. Degeneracy was shown to play an important role, especially at large gate bias. Very good agreement with available experiments was obtained, and the calculations yield a set of best-fit transport parameters.

Monte Carlo were then extended for calculations of the large-signal nonlinear response characteristics of GaN-Al_xGa_{1-x}N High Electron Mobility Transistors (HEMTs) with particular emphasis on intermodulation distortion (IMD). The nonlinear electrical transport was treated on first principles, all scattering mechanisms included, and both memory and distributed effects built into the model. The results demonstrated an optimal operating point for low intermodulation distortion (IMD) due to a minima in the IMD curve. High-temperature predictions of the IMD have also been made, by carrying out the simulations at 600 K. An increase in dynamic range with temperature has been predicted, due to a relative suppression of interface roughness scattering.

Also, a model analysis of the large-signal characteristics of GaN-Al_xGa_{1-x}N HEMTs was carried out to identify parameters and their optimal settings for enhanced microwave performance. A case has been made for increased mole fraction for the barrier layer, reducing the transit length, and introducing a thin AlN interfacial layer for suppressing real space transfer for enhancing the device performance.

The large-signal response characteristics of GaN-based Gunn oscillators have been re-examined based on recent bandstructure data that has become available for the wurtzite material. Wurtzite GaN is also more interesting since it has been shown to have a higher drift velocity that should promote higher frequencies for Gunn diode operation. Device performance parameters of interest were calculated for two separate situations. First, devices with the conventional single notch structure were simulated to obtain predictions of the output power and conversion efficiency. Then, multiple domain devices containing repetitive serial segments, were analyzed. The repetitive structure has been studied here since, to the best of our knowledge, the benefits and potential of

multiple domain structures (MDS) have not been examined in the context of GaN Gunn diodes. Theoretical predictions for GaAs Gunn oscillators call for an N^2 scaling in output power with the number of segments N .

Device parameters such as the operating frequency, power output and conversion efficiency were obtained. Variations due to changes in temperature, biasing voltage and device length were also included. As expected, the operating frequency has been shown to fall with increasing temperature due to a lower drift velocity. The results, for a single transit region structure, showed that conversion efficiencies up to about 2 percent can be attained at 300K and would be around 1.45 percent at 450 Kelvin. The room temperature value is higher than that reports for GaAs devices. Also, the efficiencies are slightly higher than those calculated elsewhere for GaN on the basis of hydrodynamic models. Corresponding peak power outputs of 0.68 W and 0.52 W have been predicted at 300 K and 450 K, respectively. Here again, considerable improvement is predicted over other material (e.g. the reported results of about 0.150 W for InP.) However, it must be emphasized that since device self-heating effects have not been included here, these values represent an overestimation.

For multiple-domain structures, considerable improvements in output power have been predicted. Without changing the device area, the output power results were seen to roughly scale with the number of segments N . Slight deviations (sub-linear behavior) seen can be attributed to the loss in absolute repetitiveness from one segment to the next. Hot electron effects and larger average carrier energies contribute to the sub-linear behavior. Hence, for devices with with scaled increases in area, the output power would not be quite as large as the predicted N^2 factor. Also, the noise for the multi-domain devices is expected to be higher than the conventional structures. This factor has not been studied and will be analyzed elsewhere. In any case, the advantage of multiple GaN Gunn diode structures has been made obvious, and such device do merit serious experimental study.

Monte Carlo studies of 2DEG transport were used to analyze carrier mobilities in wurtzite GaN HEMTs taking account of the interface polarization charges arising from edge dislocations strains and all other pertinent carrier-phonon scattering processes. Dislocation scattering has been shown to be important in bulk GaN, but has not been extensively studied in the context of GaN HEMTs. Explicit expressions for dislocation scattering were developed in the context of weak perturbation theory in the Born approximation. It was shown that dislocation scattering is anisotropic, and would have a much stronger influence at lower temperatures. For self-consistency, details of the carrier density, sub-band energies and eigenfunctions were included. This was done by including two equivalent 1×1 Hamiltonians for the ϵ_{7c} conduction bands, and a 6×6 Hamiltonian for the A , B , and C valence bands. The eigen-value information was used to calculate the scattering matrix elements using parameterized envelope wavefunctions.

Finally, electron mobilities were calculated as a function of operating temperature for various dislocation densities. The trend was shown to be in keeping with the experimental reports. Room temperature electron mobilities were predicted to be around $1.711 \times 10^3 \text{ cm}^2/\text{Vs}$, which is fairly close agreement with the data reported by the Santa Barbara group^{80,115}. At the highest dislocation density of 10^{10} cm^{-2} , mobility reduction of 16.8 percent and 8.6 percent are predicted for 77 K and 300 K, respectively. Given the sharp drop in phonon scattering at the lower temperature, the impact of dislocation scattering is relatively higher. Monte Carlo results for the electron mobility as a function of the 2DEG density were also obtained for operating temperatures of 300K and 77 K. The mobility decreased monotonically due to increased interface roughness scattering. This trend is again in keeping with experimental observations^{80,115}. The mobility decrease with density was the largest at the lower 77 K temperature, since the relative role of IRS is stronger than at 300 K.

REFERENCES

1. Y. F. Wu, B. P. Keller, S. Keller, D. Kapolnek, P. Kozodoy, S. P. Denbaars, and U. K. Mishra, Appl. Phys. Lett. **69**, 1438 (1996).

2. S. N. Mohammad, A. Salvador, and H. Morkoc, Proc. IEEE **83**, 1306 (1995).
3. H. Morkoc, *Nitride Semiconductors and Devices* (Springer-Verlag, Heidelberg, 1999).
4. R. P. Joshi, Appl. Phys. Lett. **64**, 223 (1994) ; R. P. Joshi, A. N. Dharamsi and J. Mcadoo, Appl. Phys. Lett. **64**, 3611 (1994).
5. Nakamura, T. Mukai, and M. Senoh, Appl. Phys. Lett. **64**, 1687 (1994).
6. R. Gaska, Q. Chen, J. Yang, A. Osinsky, M. A. Khan, and M. S. Shur, IEEE Electr. Dev. Lett. **18**, 492 (1997).
7. Keller, G. Parish, P. T. Fini, S. Heikman, C. H. Chen, N. Zhang, S. P. Denbaars, and U. K. Mishra, J. Appl. Phys. **86**, 5850 (1999).
8. R. Gaska, M. S. Shur, A. D. Bykhovski, A. O. Orlov, and G. L. Snider, Appl. Phys. Lett. **74**, 287 (1999).
9. K. Shenai, R. S. Scott and B. J. Baliga, IEEE Trans. Electr. Dev. **36**, 1811 (1989).
10. S. Nakamura, M. Senoh, S. Nagahama, N. Iwasa, T. Yamada, T. Matsushita, H. Kiyoku, Y. Sugimoto, T. Kozaki, H. Umemoto, M. Sano, and K. Chocho, Jpn. J. Appl. Phys. II- Lett. **36**, L1568 (1997).
11. G. E. Bulman, K. Doverspike, S. T. Sheppard, T. W. Weeks, H. S. Kong, H. M. Dieringer, J. A. Edmond, J. D. Brown, J. T. Swindell, J. F. Schetzina, Electr. Lett, **33**, 1556 (1997).
12. S. Nakamura, M. Senoh, N. Iwasa, S. Nagahama, T. Yamada, T. Mukai, Jpn. J. Appl. Phys. **34**, L1332 (1995).
13. I. J. Fritz and T. J. Drummond, Electr. Lett. **31**, 68 (1995).

14. H. Morkoc and S. N. Mohammad, "Light Emitting Diodes," *Wiley Encyclopedia of Electrical and Electronics Engineering*, edited by J. Webster (J. Wiley and Sons, New York, 1999).
15. H. Morkoc, *IEEE J. Selected Topics in Quantum Electronics* **4**, 537 (1998).
16. J. M. Barker, R. Akis, D. K. Ferry, S. M. Goodnick, T. J. Thornton, D. D. Koleske, A. E. Wickenden, and R. L. Henry, *Physica B* **314**, 39 (2002).
17. J. D. Albrecht, R. P. Wang, P. P. Ruden, M. Farahmand, and K. F. Brennan, *J. Appl. Phys.*, **83**, 4777 (1998).
18. W. F. Yu, B. P. Keller, P. Fini, J. Pysl, M. Le, N. Nguyen, C. Nguyen, D. Widman, S. Keller, S. P. Denbaars, and U. K. Mishra, *Electronics Lett.* **33**, 1742 (Sept. 1997).
19. S. T. Sheppard, K. Doverspike, W. L. Pribble, S. T. Allen, J. W. Palmour, L. T. Kehias, and T. J. Jenkins, *Electr. Dev. Lett.* **20**, 161 (1999).
20. F. Wu, B. P. Keller, S. Keller, D. Kapolnek, S. P. Denbaars, and U. K. Mishra, *IEEE Electr. Dev. Lett.* **17**, 455 (1996).
21. Y. F. Wu, D. Kapolnek, J. P. Ibbetson, P. Parikh, B. P. Keller, and U. K. Mishra, *IEEE Trans. Electr. Dev.* **48**, 586 (2001).
22. D. E. Grider, N. X. Nguyen, and C. Nguyen, *Solid State Electr.* **43**, 1473 (1999).
23. S. Rumyantsev, M. E. Levinshtein, R. Gaska, M. S. Shur, A. Khan, J. W. Yang, G. Simin, A. Ping, and T. Adesida, *Phys. Stat. Sol. A* **176**, 201 (1999).
24. G. J. Sullivan, M. Y. Chen, J. A. Higgins, J. W. Yang, Q. Chen, R. L. Pierson, and B. T. McDermott, *IEEE Electr. Dev. Lett.* **19**, 198 (1998).
25. S. C. Binari, K. Doverspike, G. Kelner, and H. B. Dietrich, *Solid St. Electr.* **41**, 177 (1997).
26. E. M. Chumbes, J. Smart, T. Prunty, and J. R. Shealy, *IEEE Trans. Electr. Dev.* **48**, 416 (2001).

27. U. Bhapkar and M. S. Shur, J. Appl. Phys. **82**, 1649 (1997).
28. J. D. Albrecht, R. P. Wang, P. P. Ruden, M. Farahmand, and K. F. Brennan, J. Appl. Phys. **83**, 4777 (1998).
29. S. T. Sheppard, K. Doverspike, W. L. Pribble, S. T. Allen, J. W. Palmour, L. T. Kehias, and T. J. Jenkins, IEEE Electr. Dev. Lett. **20**, 161 (1999).
30. G. J. Sullivan, M. Y. Chen, J. A. Higgins, J. W. Yang, Q. Chen, R. L. Pierson, and B. T. McDermott, IEEE Electr. Dev. Lett. **19**, 198 (1998).
31. K. Kim, W. R. Lambrecht, and B. Segall, Phys. Rev. B **53**, 16310 (1996).
32. T. Takeuchi, C. Wetzel, S. Yamaguchi, H. Sakai, H. Amano, I. Akasaki, Y. Kaneko, S. Nakagawa, Y. Yamaoka, and N. Yamada, Appl. Phys. Lett. **73**, 1691 (1998).
33. H. S. Kim, J. Y. Lin, H. X. Jiang, W. W. Chow, A. Botchkarev, and H. Morkoc, Appl. Phys. Lett. **73**, 3426 (1998).
34. E. A. Caridi, T. Y. Chang, K. W. Goosen, and L. F. Eastman, Appl. Phys. Lett. **56**, 659 (1990).
35. A. D. Bykhovski, V. V. Kaminski, M. S. Shur, Q. C. Chen, and M. A. Khan, Appl. Phys. Lett. **68**, 818 (1996).
36. O. Ambacher, J. Smart, J. R. Shealy, N. G. Weimann, K. Chu, M. Murphy, R. Dimitrov, L. Wittmer, M. Stutzmann, W. Rieger, and J. Hilsenbeck, J. Appl. Phys. **85**, 3222 (1999).
37. F. Bernardini, V. Fiorentini, and D. Vanderbilt, Phys. Rev. B. **56**, 10024 (1997).
38. W. Zhong, R. D. King-Smith, and D. Vanderbilt, Phys. Rev. Lett. **72**, 3618 (1994).
39. B. Doshi, K. F. Brennan, R. Bicknell-Tassius, and F. Grunthaner, Appl. Phys. Lett. **73**, 2784 (1998).
40. A. J. Sierakowski and L. F. Eastman, J. Appl. Phys. **86**, 3398 (1999).

41. T. Li, R. P. Joshi, and C. Fazi, J. Appl. Phys. **88**, 829 (2000).
42. O. Ambacher, J. Smart, J. R. Shealy, N. G. Weimann, K. Chu, M. Murphy, R. Dimitrov, L. Wittmer, M. Stutzmann, W. Rieger, and J. Hilsenbeck, J. Appl. Phys. **85**, 3222 (1999).
43. E. Alekseev and D. Pavlidis-, Solid St. Electr. **44**, 941 (2000) ; E. Alekseev and D. Pavlidis, Electr. Lett. **36**, 176 (2000).
44. S. Krishnamurthy, M. van Schilfgaarde, A. Sher, and A. B. Chen, Appl. Phys. Lett. **71**, 1999 (1997).
45. H. Eisele and G. I. Haddad, IEEE Microwave & Guided Wave Lett. **8**, 24 (1998) ; H. Eisele, A. Rydberg, G. I. Haddad, IEEE Trans. Microwave Theory Tech. **48**, 626 (2000).
46. P. J. Bulman, G. S. Hobson, and B. C. Taylor, *Transferred Electron Devices* (Academic Pres, New York, 1972).
47. J. H. Zhao, V. Gruzinskis, M. Weiner, M. Pan, P. Shiktorov, and E. Starikov, Materials Science Forum **334-342**, 1635 (2000).
48. J. Kolnick, I. H. Oguzman, K. F. Brennan, W. Rongping, P. P. Ruden, and W. Yang, J. Appl. Phys. **78**, 1033 (1995).
49. B. E. Foutz, S. K. O'Leary, M. S. Shur, and L. F. Eastmen, J. Appl. Phys. **85**, 7727 (1999).
50. W. R. L. Lambrecht and B. Segall, in *Properties of Group III Nitrides*, EMIS Datareviews Series, No. 11, edited by J. H. Edgar (Inspec, London, 1994), Chap. 4.
51. M. Goano, E. Bellotti, E. Ghillino, G. Ghione, and K. F. Brennan, J. Appl. Phys. **88**, 6467 (2000).
52. P. Lugli and D. K. Ferry, IEEE Trans. Elec. Dev. **32**, 2431 (1985).

53. J. D. Albrecht, R. P. Wang, P. P. Ruden, M. Farahmand, and K. F. Brennan, *J. Appl. Phys.* **32**, 4777 (1998).
54. O. Madelung, in *Physics of Group IV Elements and III-V Compounds*, Group III, Vols. 17a and 22a, Landolt-Bornstein New Series (Springer-Verlag, Berlin, 1981).
55. A. G. Sabnis and J. T. Clemens, *IEDM Tech. Digest*, pp.18-21, (1979).
56. U. Ravaioli and D. K. Ferry, *IEEE Trans. Elec. Dev.* **33**, 677 (1986).
57. R. P. Joshi, *Appl. Phys. Lett.* **72**, 2156 (1998).
58. W. Walukiewicz, H. E. Ruda, J. Lagowski, and H. C. Gatos, *Phys. Rev. B.* **30**, 4571 (1984).
59. T. Ando, A. B. Fowler and F. Stern, *Rev. Mod. Phys.* **54**, 437 (1982).
60. F. F. Fang and W. E. Howard, *Phys. Rev. Lett.* **16**, 797 (1966).
61. D. K. Ferry, *Phys. Rev. B* **14**, 1605 (1976).
62. S. Yamakawa, H. Ueno, K. Taniguchi, C. Hamaguchi, K. Miyatsuji, K. Masaki, and U. Ravaioli, *J. Appl. Phys.* **79**, 911 (1996).
63. L. Hsu and W. Walukiewicz, *Phys. Rev. B* **56**, 1520 (1997).
64. S. Mori and T. Ando, *Phys. Rev. B* **19**, 6433 (1979).
65. S. M. Goodnick, D. K. Ferry, C. W. Wilmsen, Z. Lilienthal, D. Fathy, and O. L. Krivanek, *Phys. Rev. B* **32**, 8171 (1985).
66. Y. Zhang and J. Singh, *J. Appl. Phys.* **85**, 587 (1999).
67. D. Vasileska and D. K. Ferry, *IEEE Trans. Elec. Dev.* **ED-44**, 577 (1997).
68. F. Bernardini, V. Fiorentini, and D. Vanderbilt, *Phys. Rev. B.* **56**, 10024 (1997).

69. L. S. Yu, D. J. Qiao, Q. J. Xing, S. S. Lau, K. S. Boutros, and J. M. Redwing, Appl. Phys. Lett. **73**, 238 (1998).
70. J. D. Albrecht, R. P. Wang, P. P. Ruden, M. Farahmand, and K. F. Brennan, J. Appl. Phys. **32**, 4777 (1998).
71. G. Martin, A. Botchkarev, A. Rockett, and H. Morkoc, Appl. Phys. Lett. **68**, 2541 (1996).
72. X. H. Wu, L. M. Brown, D. Kapolnek, S. Keller, B. Keller, S. P. DenBaars, and J. S. Speck, J. Appl. Phys. **80**, 3228 (1996).
73. C. Shi, P. M. Asbeck, and E. T. Yu, Appl. Phys. Lett. **74**, 573 (1999).
74. D. Jena, A. C. Gossard, and U. K. Mishra, Appl. Phys. Lett. **76**, 1707 (2000).
75. H. M. Ng, D. Doppalapudi, T. D. Moustakas, N. G. Weimann, and L. F. Eastman, Appl. Phys. Lett. **73**, 821 (1998).
76. S. Keller, B. P. Keller, Y. F. Wu, B. Heying, D. Kapolnek, J. S. Speck, U. K. Mishra, and S. P. Denbaars, Appl. Phys. Lett. **68**, 1525 (1996).
77. D. C. Look and J. R. Sizelove, Phys. Rev. Lett. **82**, 1237 (1999).
78. J. L. Farvacque, Z. Bougrioua, I. Moerman, G. Van Tendeloo, and O. Lebedev, Physica B **273-274**, 140 (1999).
79. J. L. Farvacque, Z. Bougrioua, and I. Moerman, Phys. Rev. B **63**, 115202 (2001).
80. Keller, G. Parish, P. T. Fini, S. Heikman, C. H. Chen, N. Zhang, S. P. Denbaars, and U. K. Mishra, J. Appl. Phys. **86**, 5850 (1999).
81. E. D. Siggia and P. C. Kwok, Phys. Rev. B **2**, 1024 (1970).
82. F. Stern, Phys. Rev. Lett. **18**, 546 (1967).
83. A. L. Fetter, Phys. Rev. B **10**, 3739 (1974).
84. B. Jogai, to appear J. Appl. Phys., Feb. 2003.
85. R. P. Joshi and R. F. Wood, J. Appl. Phys. Lett. **84**, 3197 (1998) ; R. P. Joshi and R. F. Wood, J. Appl. Phys. **83**, 5543 (1998).
86. D. Jena and U. K. Mishra, Appl. Phys. Lett. **80**, 64 (2002).

87. H. Morkoc, A. Di Carlo, and R. Cingolani, *Solid State Electr.* **46**, 157 (2002).
88. J. P. Ibbetson, P. T. Fini, K. D. Ness, S. P. DenBaars, J. S. Speck, and U. K. Mishra, *Appl. Phys. Lett.* **77**, 250 (2000).
89. T. Li, R. P. Joshi, and R. del Rosario, *IEEE Trans. Electr. Dev.* **49**, 1511 (2002).
90. R. P. Joshi and D. F. Ferry, *Phys. Rev. B* **43**, 9734 (1991).
91. S. L. Chuang, *Phys. Rev. B.* **43**, 9649 (1991).
92. T. Ando, A. B. Fowler, and F. Stern, *Rev. Mod. Phys.* **54**, 437 (1982).
93. M. Abramowitz and I. A. Stegun, *Handbook of Mathematical Functions* (Dover, New York, 1972).
94. B. Jogai, *J. Appl. Phys.* **91**, 3721 (2002).
95. B. Jogai, *Phys. Stat. Sol. B* **233**, 506 (2002).
96. J. C. Pedro and N. B. de Carvalho, *IEEE Trans. Microwave Theory Tech.* **47**, 2393 (1999).
97. J. A. Higgins and R. L. Kuvas, *IEEE Trans. Microwave Theory Tech.* **28**, 9 (1980).
98. M. J. Bailey, *IEEE Transactions on Microwave Theory and Techniques* **48**, 104 (2000).
99. Trofimenkoff, *Proc. IEEE* **53**, 1765 (1965).
100. J. Kolník, I. H. Oguzman, K. F. Brennan, R. Wang, P. P. Ruden, and Y. Wang, *J. Appl. Phys.* **78**, 1033 (1995).
101. J. L. Thobel, A. Sleiman, and R. Fauquembergue, *J. Appl. Phys.* **82**, 1220 (1997); P. Borowik and J. L. Thobel, *J. Appl. Phys.* **87**, 329 (2000).
102. T. Yamada, H. Miyata, J. R. Zhou, and D. K. Ferry, *Phys. Rev. B* **49**, 1875 (1994).
103. B. R. Nag, in *Electron Transport in Compound Semiconductors* (Springer, Berlin, 1980).

104. R. Dimitrov, L. Wittmer, H. P. Felsl, A. Mitchell, O. Ambacher, and M. Stutmann, *Phys. Stat. Sol. A* **168**, 7 (1998).
105. S. C. Binari, J. M. Redwing, G. Kelner, and W. Kruppa, *Electr. Lett.* **33**, 242 (1997).
106. C. Nguyen, N. X. Nguyen, M. Le, and D. E. Grider, *Electr. Lett.* **34**, 309 (1998).
107. L. W. Wong, S. J. Cai, K. Wang, H. W. Jiang, and M. Chen, *Appl. Phys. Lett.* **73**, 1391 (1998).
108. Y. Fu, K. B. Joelsson, K. J. Grahm, W. X. Ni, G. V. Hansson, and M. Willander, *Phys. Rev. B* **54**, 11317 (1996).
109. For example, M. Schetzen, in *The Volterra and Wiener Theories of Nonlinear Systems* (Wiley, New York, 1980).
110. L. Shen, S. Heikman, B. Moran, R. Coffie, N. Q. Zhang, D. Buttari, I. P. Smorchkova, S. Keller, S. P. DenBaars, and U. K. Mishra, *IEEE Electr. Dev. Lett.* **22**, 457 (2001).
111. P. A. Blakey and R. K. Froelich, *IEEE Trans. Microwave Theory Tech.* **31**, 781 (1983).
112. R. Vaidyanathan and R. P. Joshi, *IEE Electr. Lett.*, **27**, 1555 (1991).
113. C. Lee and U. Ravaioli, *IEE Electr. Lett.*, **26**, 425 (1990).
114. V. Gruzinskis, E. Starikov, P. Shiktorov, L. Reggiani, and L. Varani, *J. Appl. Phys.* **76**, 5260 (1994).
115. C. R. Elsass, I. P. Smorchkova, B. Heying, E. Haus, P. Fini, K. Maranowski, J. P. Ibbetson, S. Keller, P. M. Petroff, S. P. DenBaars, U. K. Mishra, and J. S. Speck, *Appl. Phys. Lett.* **74**, 3528 (1999).
116. H. W. Thim, *J. Appl. Phys.* **39**, 3898 (1968).